

LY α RADIATIVE TRANSFER: MODELING SPECTRUM AND SURFACE BRIGHTNESS PROFILE OF LY α -EMITTING GALAXIES AT $Z=3-6$

HYUNMI SONG^{1,2}, KWANG-IL SEON^{2,3}, AND HO SEONG HWANG²

¹Department of Astronomy, Yonsei University, 50 Yonsei-ro, Seodaemun-gu, Seoul 03722, Republic of Korea

²Korea Astronomy & Space Science Institute, Daedockdae-ro 776, Yuseong-gu, Daejeon 34055, Republic of Korea

³Astronomy and Space Science Major, University of Science and Technology, Daejeon 34113, Republic of Korea

ABSTRACT

We perform Ly α radiative transfer calculations for reproducing Ly α properties of star-forming galaxies at high redshifts. We model a galaxy as a halo in which the density distributions of Ly α sources and H I plus dust medium are described with exponential functions. We also consider an outflow of the medium that represents a momentum-driven wind in a gravitational potential well. We successfully reproduce both the spectra and the surface brightness profiles of eight star-forming galaxies at $z=3-6$ observed with MUSE using this outflowing halo model with Ly α scattering. The best-fit model parameters (i.e., the outflowing velocity and optical depth) for these galaxies are consistent with other studies. We examine the impacts of individual model parameters and input spectrum on emerging spectrum and surface brightness profile. Further investigations on correlations among observables (i.e., the spatial extent of Ly α halos and Ly α spectral features) and model parameters, and spatially resolved spectra are presented as well. We demonstrate that the combination of spectrum and surface brightness profile provides strong constraints on model parameters and thus spatial/kinematic distributions of medium.

Keywords: galaxies: high-redshift – galaxies: kinematics and dynamics – radiative transfer – scattering

1. INTRODUCTION

Ly α emission is one of the most prominent emission features in the universe. It is usually generated by the interplay between atomic hydrogen (H I, the most common element in the universe) and ionizing photons from young stars. It was expected that one would detect strong Ly α emission from star-forming galaxies and can use it to probe even the first generation of galaxies at high redshifts (Partridge & Peebles 1967; Sunyaev et al. 1978). However, it had been unsuccessful to detect Ly α emission from either nearby galaxies or high-redshift galaxies. Meier & Terlevich (1981) did the first attempt to search for Ly α emission in nearby H II-selected galaxies, and found Ly α emission in only one galaxy; the first detection of high-redshift Ly α emitters that are not physically associated with quasars was made in 1998 by Cowie & Hu (1998).

Such difficulties in detecting Ly α emission are because of particular technical requirements; space telescopes for nearby sources and high detection sensitivities for high-redshift sources are necessary for good detection. However, it is also due to the resonance scattering nature of Ly α ; Ly α photons are endlessly scattered off by neutral hydrogen atoms until they happen to be scattered into wing frequencies, which occurs quite rarely. Ly α photons are forced to travel long distances in the H I medium and have a high chance to be destructed by dust, which eventually suppresses the observed intensity. In addition, this whole process is sensitive to the spatial and kinematic distributions of the H I medium, so it is not easy to understand the observed correlations between physical parameters (e.g., between Ly α intensity and metallicity, Ly α intensity and UV continuum flux, etc.) nor to make observational predictions (Meier & Terlevich 1981; Hartmann et al. 1988; Neufeld 1990; Charlot & Fall 1993; Valls-Gabaud 1993; Kunth et al. 1998; Tenorio-Tagle et al. 1999; Mas-Hesse et al. 2003).

Nevertheless, there have been continuous efforts to search for Ly α emission from the observation side. There are targeted observations for individual objects as well as large photometric and spectroscopic surveys. Such Ly α surveys include the Large Area Lyman Alpha survey (LALA, Rhoads et al. 2000), the Ly α Reference Sample survey (LARS, Östlin et al. 2014), the Subaru Deep Field survey (e.g., SILVERRUSH, Ouchi et al. 2018), and the survey with Multi-Unit Spectroscopic Explorer (MUSE, Bacon et al. 2015). The MUSE at the ESO-VLT is the latest technological advances with 24 integral field units and unprecedented sensitivity. There are several recent observations with

MUSE that reveal ubiquitous Ly α emission in the universe (Bacon et al. 2015; Wisotzki et al. 2016; Drake et al. 2017; Leclercq et al. 2017).

Observations have shown that the shape of Ly α line is diverse, which includes broad damped absorption profiles, P-Cygni profiles, double-peak profiles, pure symmetric emission profiles, and combinations thereof (Kunth et al. 1998; Mas-Hesse et al. 2003; Shapley et al. 2003; Møller et al. 2004; Venemans et al. 2005; Wilman et al. 2005; Noll et al. 2004; Tapken et al. 2004). Such a variety can be understood through a detailed radiative transfer calculation, which is analytically solvable only for simple cases (e.g., a static, plane-parallel slab by Harrington 1973 and Neufeld 1990, a static uniform sphere by Dijkstra et al. 2006a). Later, numerical algorithms based on Monte Carlo techniques had been developed to solve radiative transfer for more general cases. Now theoretical studies mostly rely on them (e.g., Spaans 1996; Loeb & Rybicki 1999; Ahn et al. 2000, 2002; Zheng & Miralda-Escudé 2002; Richling 2003; Cantalupo et al. 2005; Dijkstra et al. 2006b; Hansen & Oh 2006; Tasitsiomi 2006; Verhamme et al. 2006; Laursen et al. 2013; Behrens et al. 2014; Duval et al. 2014; Gronke et al. 2015; Verhamme et al. 2015; Michel-Dansac et al. 2020). Meanwhile, a galaxy model needs to be constructed to perform such a radiative transfer calculation. One can adopt a realistic galaxy model from hydrodynamical simulations. Galaxies from such simulations can be useful for performing a statistical study of Ly α properties, but they can not be directly used to model individual galaxies in observations. Therefore, it would be better to adopt a simple but manageable toy model for the purpose of reproducing observations. One example for such models is a shell model, in which a central Ly α source is surrounded by an constantly-expanding, homogeneous, spherical shell of H I medium with dust. Although this shell model has surprisingly well reproduced many observed Ly α line profiles (e.g., Ahn 2004; Schaerer & Verhamme 2008; Verhamme et al. 2008; Schaerer et al. 2011; Gronke et al. 2015; Yang et al. 2016; Karman et al. 2017; Gronke 2017), because of its extreme simplicity and contrivance, there are still rooms to improve (e.g., see Section 7.2 in Yang et al. 2016; Orlitová et al. 2018).

On the other hand, there are other observables than spectrum, which are not yet fully understood. Dijkstra & Kramer (2012) is one of few studies that focused on reproducing observed Ly α absorption features in the spectra of background galaxies and Ly α halos around star-forming galaxies by considering a galaxy model with outflowing clumpy medium. Here, Ly α halos denote the spatial distribution of Ly α emission that is much more extended than that of stellar UV continuum or H α (e.g., Fynbo et al. 1999; Steidel et al. 2011; Matsuda et al. 2012; Hayes et al. 2013; Yang et al. 2017). This indicates rich gas content in the circumgalactic medium (CGM). Thus, Ly α halos might provide us the information on the spatial distribution and kinematics of the CGM, which is important for understanding galaxy formation and evolution. However, Ly α halos were detectable usually in a stacked image because of their low surface brightness (Steidel et al. 2011; Momose et al. 2014, 2016). Thanks to the MUSE observations that revealed ubiquitous Ly α halos around star-forming galaxies at high redshifts (Wisotzki et al. 2016; Leclercq et al. 2017), we can now study Ly α halos for individual galaxies, and even the spatial variations of their spectral properties (Erb et al. 2018; Claeysens et al. 2019; Leclercq et al. 2020)

Therefore we are in a good position to fit both Ly α spectrum and Ly α surface brightness profile for individual high-redshift star-forming galaxies, and to test a galaxy model with Ly α radiative transfer. In this study, we construct a galaxy toy model that is improved from the shell model to better represent real galaxies: a halo in which the density distributions of Ly α sources and H I plus dust medium, as well as medium bulk motion, are modeled with free parameters. We perform Ly α Monte Carlo radiative transfer calculations with this galaxy model for a number of model parameter sets. We then find a parameter set that best reproduces both the observed Ly α spectrum and surface brightness profile of high-redshift star-forming galaxies reported in Leclercq et al. (2017) (hereafter L17). We discuss the advantage of simultaneous use of these two observables in constraining models, and examine various correlations among model parameters and observables. We also explore spatially resolved Ly α spectra, and the impact of input Ly α spectrum on emerging Ly α spectrum and surface brightness profile.

This paper is constructed as follow. In Section 2, we describe our Ly α Monte Carlo radiative transfer simulation, the galaxy model, the observational data to fit, and the fitting process. We present the best-fit results for the galaxy sample in Section 3. Further discussions and summaries are presented in Sections 4 and Section 5, respectively.

2. METHOD

2.1. Ly α Monte Carlo Radiative Transfer

We describe Ly α Monte Carlo radiative transfer calculations we perform in this section. We use a code called LaRT¹ (Lyman- α Radiative Transfer, Seon & Kim 2020). It is written in modern Fortran with the Message Passing Interface, and is enabled to consider arbitrary three-dimensional distributions for density, temperature, and kinematics of sources

¹ <https://seoncafe.github.io/LaRT.html>

and medium on a regular Cartesian grid. We set a 128^3 grid, which gives a physical resolution of ~ 0.2 kpc. In the code, we generate and track photons (or photon packets) in real and frequency spaces for a given simulation parameter set. The calculation is performed by distributing photons over processors and later is summed together. The master-slave algorithm is used to implement dynamic load balancing. The code was extensively tested to reproduce the well-known benchmark cases for static slab and spherical geometries as well as for Hubble-like expanding spherical media. The test was performed not only in hydrogen-only media but also in dusty media. The procedures performed in the code for each photon are as follows.

1. We generate a photon with a position vector \mathbf{r} , a direction vector \mathbf{k} , and a frequency ν drawn from a Ly α source spatial distribution function under consideration, an isotropic distribution function, and a Ly α input frequency distribution function of interest, respectively.
2. We randomly choose a τ value following a probability distribution of $\exp(-\tau)$ to determine the traveling distance ℓ for the photon through the relation $\tau = \int_0^\ell (\sigma_{\text{H I}} n_{\text{H I}}(\mathbf{x}) + \sigma_{\text{d}} n_{\text{d}}(\mathbf{x})) d|\mathbf{x}|$ where σ and n represent the cross section and the number density of atomic hydrogen (H I) or dust (d), respectively. The optical depth due to hydrogen atoms is calculated using the Voigt routine in the VPFIT package (Carswell & Webb 2014).
3. The position of the photon is updated to $\mathbf{r} + \ell\mathbf{k}$. At the new position, we decide which of the two (hydrogen and dust) the photon will interact with by considering the probabilities given by their optical depths to the total optical depth. If the photon interacts with hydrogen (i.e., the photon being scattered), a new direction vector is drawn from the Rayleigh phase function. Then, the velocity components of the scattering atom are drawn from a function given by Eqn. (4) of Zheng & Miralda-Escudé (2002) and the Maxwell-Boltzmann distribution (see Seon & Kim 2020, for more details). This velocity of the scattering atom and the old and new direction vectors of the photon determine a new frequency following the energy-momentum conservation law. If it interacts with dust, the photon will be either scattered with the probability of a (dust albedo) or absorbed with the probability of $1-a$. When the photon is scattered by dust, the frequency is not changed, and a new direction is drawn from a proper angular redistribution function (the Henyey-Greenstein phase function by default, Henyey & Greenstein 1941; Witt 1977).
4. We repeat Steps 2 and 3 until either the photon escapes the system considered (i.e., a galaxy) or is absorbed by dust. Then, we go to Step 1 for a new photon.

Although the absorption and scattering by dust can be explicitly simulated using our code with various choices of albedo and scattering phase function as described in Step 3, we post-process the effect of dust to reduce the computational time. Whenever each photon escapes the galaxy, we record its initial position (r_i), initial frequency (ν_i), cumulative (the photon has gone through) hydrogen optical depth ($\hat{\tau}_{\text{H I}}$), cumulative hydrogen column density ($\hat{N}_{\text{H I}}$), final (projected) position in the observed image (R_f), final frequency (ν_f), and distance to an observer from the final position (d_{obs}). The initial position/frequency and the cumulative hydrogen column density are particularly recorded for post-processing the spatial/frequency distributions of Ly α source and dust effect. Such post-processing is adopted to reduce the number of simulation runs that are required to study the effect of the three. Following Gronke et al. (2015), we post-process the spatial/frequency distributions of Ly α and dust effect by adjusting the weight (w) of each photon to

$$w = \frac{\mathcal{R}_f(r_i) \mathcal{S}_f(\nu_i)}{\mathcal{R}_i(r_i) \mathcal{S}_i(\nu_i)} \exp(-(1-a)\tilde{\sigma}_{\text{d,MW}} \hat{N}_{\text{H I}} \text{DGR}/\text{DGR}_{\text{MW}}). \quad (1)$$

\mathcal{R} and \mathcal{S} are the input spatial and spectral distributions of Ly α sources, respectively. Here the subscripts i and f indicate the initial (that is chosen as an input for the simulation run) and final choices, respectively. $\text{DGR}/\text{DGR}_{\text{MW}}$ is the amount of dust relative to gas (dust-to-gas ratio, DGR) normalized by the value of the Milky Way, and $\tilde{\sigma}_{\text{d,MW}}$ is the dust cross section *per neutral hydrogen* of the Milky Way, which is the product of $\sigma_{\text{d,MW}}$ and DGR_{MW} . Our choices of \mathcal{R}_i and \mathcal{S}_i are uniform distribution functions of r and ν , respectively, within given ranges, which can be easily modified for other distributions through post-processing. The exponential term can be simply rewritten as $\exp(-(1-a)\hat{\tau}_{\text{d}})$, which depicts how much fraction of each photon would not be destructed by dust, but be survived after its travel in the galaxy. In the post-processing, we assume that dust scatters photons to the direction of its original propagation (perfect forward scattering), of which validation is presented in Appendix A. At far ultraviolet wavelengths, scattering is indeed strongly forward-directed (Seon & Draine 2016). The dust extinction cross-section and albedo of the Milky Way are $\tilde{\sigma}_{\text{d,MW}} = 1.61 \times 10^{-21} \text{ cm}^2/H$ and $a_{\text{MW}} = 0.325$, respectively (Weingartner & Draine 2001; Draine 2003).

To make observables, we use the information of *all* photons at the moment when each of them escapes the galaxy. This method works because we set the system to be spherically symmetric (Section 2.2), and thus observation from all directions will be identical.

2.2. Galaxy Model

We construct a galaxy model by improving the widely used shell model, which is more realistic but still simple. We adopt a spherically symmetric halo model for the distribution of hydrogen atom (no deuterium) plus dust medium, of which density follows an exponential function with a scale radius ($rs_{\text{H I}}$) that is a free parameter. The overall density level is another free parameter, that is the optical depth from the center to the edge of the halo for a photon at the Ly α central frequency (τ_0 ²). We fix the medium temperature at 10^4K .

We assume that all the Ly α photons are generated through recombinations of electrons and hydrogen ions that are ionized by UV photons from young stars (i.e., H II regions around young stars). We thus model the spatial distribution of Ly α sources using the observed UV continuum surface brightness profiles. The UV surface brightness profile of the target galaxies in this study is well described by an exponential function of the projected distance from the galaxy center (see the rightmost panels of Figures 2 and 3 in L17), which is reconstructed as a modified Bessel function of the second kind with $n = 0$ ($K_0(x)$) when the distance is measured in three-dimensional space. We therefore assume that the spatial distribution of Ly α sources follows $K_0(r/rs_{\text{cont}})$ where rs_{cont} is the scale radius of the UV continuum surface brightness profile. Ly α photons are assumed to follow a Voigt profile with temperature 10^4K (a typical value for H II regions) in frequency space. As mentioned in Section 2.1, the spatial and frequency distributions of Ly α photons are post-processed with Eqn. (1) by inserting the Bessel function and the Voigt function for \mathcal{R}_f and \mathcal{S}_f , respectively.

We consider the bulk motion of the medium as most preexisting models do. An observed Ly α emission line is typically singly red-peaked or red-peak dominated, which are expected to emerge from outflowing medium (e.g., Verhamme et al. 2006, 2008; Vanzella et al. 2010). There are other observational evidences such as the offsets between redshifts of interstellar absorption lines, Ly α lines, and nebular emission lines (Steidel et al. 2010, and references therein), and blueshifted absorption and redshifted emission for resonance lines (Prochaska et al. 2011, and references therein). In particular, we employ an outflow model in which velocity increases and then decreases as radial distance from the center increases. This is motivated by Dijkstra & Kramer (2012, see their Section 6.1 and references therein) to describe a momentum-driven wind from the center that is decelerating in the galactic gravitational potential well. However, instead of adopting a functional form by solving a momentum equation in a gravitational potential well as in Dijkstra & Kramer (2012), we rather consider a linearly increasing and then decreasing function for simplicity. It is expressed as

$$V(r) = \begin{cases} V_{\text{peak}} r/r_{\text{peak}} & \text{if } r \leq r_{\text{peak}} \\ V_{\text{peak}} + \Delta V (r - r_{\text{peak}})/(r_{\text{max}} - r_{\text{peak}}) & \text{if } r > r_{\text{peak}} \end{cases} \quad (2)$$

where V_{peak} , r_{peak} , and ΔV are the peak velocity, the radius where velocity reaches the peak value, and the velocity difference between those at r_{max} and r_{peak} (ΔV is allowed in the range between $-V_{\text{peak}}$ and 0 to represent decelerated outflowing motion but prevent inflowing motion), which are free parameters in our galaxy model. It should be noted that in our model the initial generation of Ly α photons is not from this expanding medium (i.e., non-comoving sources). Therefore, the frequency of Ly α photons observed by a hydrogen atom in the medium will be seen shifted by the amount that is proportional to the medium velocity.

The abovementioned five free parameters ($rs_{\text{H I}}$ and τ_0 for medium density structure, V_{peak} , r_{peak} , and ΔV for medium kinematic structure) are simulation parameters, each of which is assigned a value from a range of interest for a simulation run. In addition, the relative amount of dust with respect to gas (DGR) and redshift (z) of a model galaxy are also considered as free parameters in our model. Their effects are implemented through post-processing, so called post-processing parameters. In post-processing, the weight of each photon in a simulation output is adjusted following Eqn. (1) for a chosen DGR value, and their final wavelengths are redshifted by a factor of $1 + z$ in the observer's frame due to the cosmic expansion. Simulated observables are constructed in the observer's frame.

Table 1 shows the parameter grid of simulation. The simulation is run on the grid of the five simulation parameters, and outputs are additionally post-processed on the grid of the two post-processing parameters. In total, we run 13,230 simulations with 10^6 photons per simulation, and each simulation is post-processed over additional 110 post-processing parameter grid points.

² The subscript, 0, indicates the Ly α central frequency.

Table 1. Parameter Grid of Simulation

Parameter	Values
r_{HI}^{a}	[0.1, 0.2, 0.3, 0.4, 0.5, 0.6, 0.7, 0.8, 0.9]
$r_{\text{peak}}^{\text{b}}$	[0.0, 0.1, 0.2, 0.3, 0.4, 0.5, 0.6]
$V_{\text{peak}}^{\text{c}}$	[100, 200, 300, 400, 500]
ΔV^{d}	[-500, -450, -400, ..., -100, -50, 0]
$\log \tau_0^{\text{e}}$	[5.7, 6.0, 6.3, 6.6, 6.9, 7.2]
DGR $^{\text{f}}$	[0.0, 0.2, 0.4, ..., 1.6, 1.8, 2.0]
z^{g}	$z_0 + [0.001, 0.002, 0.003, \dots, 0.008, 0.009, 0.010]$

NOTE—If it is not mentioned, each parameter is in the unit stated here for the rest of the paper.

^aThe scale radius of the medium density distribution that is described by an exponential function. It is in the normalized unit by the maximum scale of the system (r_{max}) we set in the simulation. All the length scales in this study are in the normalized unit by r_{max} .

^bThe radius when the expanding velocity of the medium reaches its peak, in the normalized unit by r_{max} .

^cThe peak velocity of the expanding velocity profile of the medium in the unit of km s^{-1} .

^dThe difference between the velocities at r_{max} and V_{peak} in the unit of km s^{-1} . ΔV is allowed in the range between $-V_{\text{peak}}$ and 0.

^eThe optical depth measured at the Ly α central frequency, which is given by the product of the hydrogen column density of the system and the cross section of a Ly α photon at the central frequency with a neutral hydrogen atom.

^fDust-to-Gas Ratio, which is the amount of dust relative to gas (in terms of mass). It is in the normalized unit by the value of the Milky Way (DGR $_{\text{MW}}$).

^gRedshift. z_0 is an approximate estimate for the redshift of the system derived from observation.

2.3. Observational Data and Fitting Procedure

The targets that we aim to model with our simulation are taken from L17. They investigated 250 Lyman Alpha Emitters (LAEs) in the *Hubble* Ultra Deep Field, which were observed with the MUSE to study the extended Ly α halo around individual galaxies. Because the MUSE covers a wavelength range between 4750Å and 9350Å, the targeted LAEs are mainly at a redshift range $2.75 \lesssim z \lesssim 6.5$. L17 summarized all the measurements from their analysis in Table B.1, which are good enough to fully reconstruct observed surface brightness profiles, but not spectra (only equivalent width (EW) and full width at half maximum (FWHM) of Ly α lines are available in their table). Therefore, we use only 14 LAEs for which Ly α spectrum and surface brightness profile are fully presented in their Figures 2 and 3, as a pilot study. Because we set an outflow model to reproduce red peak-dominated spectra that are typical Ly α features in observations, we exclude three LAEs with double-peak spectrum (MUSE #1087, 106, and 6297). We also exclude three LAEs with few (less than 15) data points in their surface brightness profiles; two of which have no counterparts in the UV continuum (MUSE #6498, 6534, and 218). In the result, we have eight LAEs, which are MUSE #1185, 82, 6905, 1343, 53, 171, 547, and 364. We read data points of their spectrum and surface brightness profile using **Engauge Digitizer**³, a free software that extracts data points from images with graphs.

On the simulation side, we construct a spectrum and a surface brightness profile by counting photons (with their weight) in a given wavelength bin and a radial bin, respectively. To better match the observation, it is necessary to follow the actual observational setups including the aperture for spectrum, imaging band width, spectral resolution, and point spread function (PSF). Following the processes described in L17, we apply their aperture size (r_{lim} , the white contour in the second column of their Figures 2 and 3) and imaging band width (the purple shaded range in the third column) when we count photons to construct spectrum and surface brightness profile, respectively. We also convolve the spectrum with a Gaussian kernel with the MUSE spectral resolution of $R \sim 3000$, and convolve the surface

³ <http://markummitchell.github.io/engauge-digitizer/>

Table 2. Observed Properties of Our Target Galaxies

MUSE #	$r_{s\text{cont}}^a$	r_{lim}^b	$[\lambda_1, \lambda_2]^c$	$\langle S/N \rangle_{\text{sp}}^d$	$\langle S/N \rangle_{\text{SBP}}^e$	$\langle S/N \rangle_{\text{tot}}^f$
1185	0.041	0.24	[6681.179, 6692.522]	7.747	7.051	7.482
82	0.017	0.20	[5598.684, 5611.14]	3.344	6.025	4.327
6905	0.029	0.20	[4982.524, 4990.045]	3.835	4.096	3.943
1343	0.016	0.20	[6038.929, 6050.097]	1.427	2.070	1.748
53	0.030	0.24	[7021.233, 7029.938]	10.158	7.192	9.205
171	0.025	0.24	[5934.927, 5941.174]	2.471	4.171	3.168
547	0.011	0.24	[8477.564, 8486.28]	3.891	4.398	4.103
364	0.014	0.24	[6004.97, 6009.919]	1.213	3.008	1.801

^aScale radius of UV continuum radial profile in the unit of r_{max} . Borrowed from $r_{s\text{cont}}$ in Figure 4 (also see Table B.1) in L17.

^bAperture size for spectrum obtained by roughly measuring the radius of the HST segmentation mask that is convolved with the MUSE PSF (white contour in each panel of the second column of Figures 2 and 3 in L17).

^cWavelength range for surface brightness profile (i.e., image bandwidth) that corresponds to the purple area in each panel of the third column of Figures 2 and 3 in L17.

^dMean signal-to-noise of observed spectrum data

^eMean signal-to-noise of observed surface brightness profile data

^fMean signal-to-noise of observed spectrum and surface brightness profile data

brightness profile with a Moffat kernel with a fixed power index (β) of 2.8 and the MUSE PSF FWHM $\sim 0.7''$. The MUSE spectral resolution and PSF FWHM are dependent on wavelength, but the dependence is weak (Bacon et al. 2017). Therefore we ignore their wavelength dependence for simplicity. The aperture size (r_{lim}) applied to each MUSE galaxy is summarized in Table 2 together with the scale radius of the UV surface brightness profile ($r_{s\text{cont}}$). Both are in the unit normalized by r_{max} that is the maximum angular extent of $5''$ as displayed in Figures 2 and 3 in L17, and that corresponds to the maximum angular size of the galaxy in the simulation.

To quantify how well the spectrum and the surface brightness profile of simulation describe the observational data, we define a likelihood as

$$\ln \mathcal{L} \propto -\frac{1}{2} \sum_i \left(\frac{O_i - M_i}{\sigma(O_i)} \right)^2. \quad (3)$$

Here, i denotes i -th bin (a wavelength bin for spectrum and a radial bin for surface brightness profile), O and M denote values from observation and model, respectively, and $\sigma(O)$ is the error in observational data. Assuming that spectrum and surface brightness profile are independent from each other, the total likelihood (\mathcal{L}_{tot}) of a model with a given parameter set can be defined by a product of the likelihoods of spectrum and surface brightness profile (\mathcal{L}_{sp} and \mathcal{L}_{SBP} , respectively, and the subscripts sp and SBP for spectrum and surface brightness profile, respectively). By calculating \mathcal{L}_{tot} for all permitted parameter sets, we construct a surface of \mathcal{L}_{tot} in the seven (five simulation parameters plus two post-processing parameters) dimensional parameter space. Then, we derive a one-dimensional (1D) (marginal) posterior distribution of a parameter and a two-dimensional (2D) (marginal) posterior map of two parameters by marginalizing over other parameters assuming uniform priors. A best-fit parameter is found as the value where the maximum of its 1D posterior distribution appears, and the degeneracy between parameters is inferred from 2D posterior maps. We note that the normalizations of the simulated spectrum and the simulated surface brightness profile are adjusted arbitrarily to minimize the difference between model and observation. *Because we compare only their shapes, a parameter that is more sensitive to the absolute levels (e.g., DGR) could be poorly constrained by our modeling.*

The error of each best-fit value is roughly measured as follows. We linearly connect adjacent \mathcal{L} values and adjust the normalization to make the area below the \mathcal{L} profile within the allowed parameter range be 1. We then make a 1σ range that includes a best-fit value and covers 68% of the total area.

3. RESULTS: FIT TO OBSERVED Ly α SPECTRA AND SURFACE BRIGHTNESS PROFILES

In this section, we show 1D and 2D posterior distributions of the seven parameters, constraints on their best-fit value, and the corresponding best model spectrum and surface brightness profile for each of our eight target galaxies. We first fit spectrum and surface brightness profile separately (Section 3.1), and later fit both simultaneously (Section 3.2).

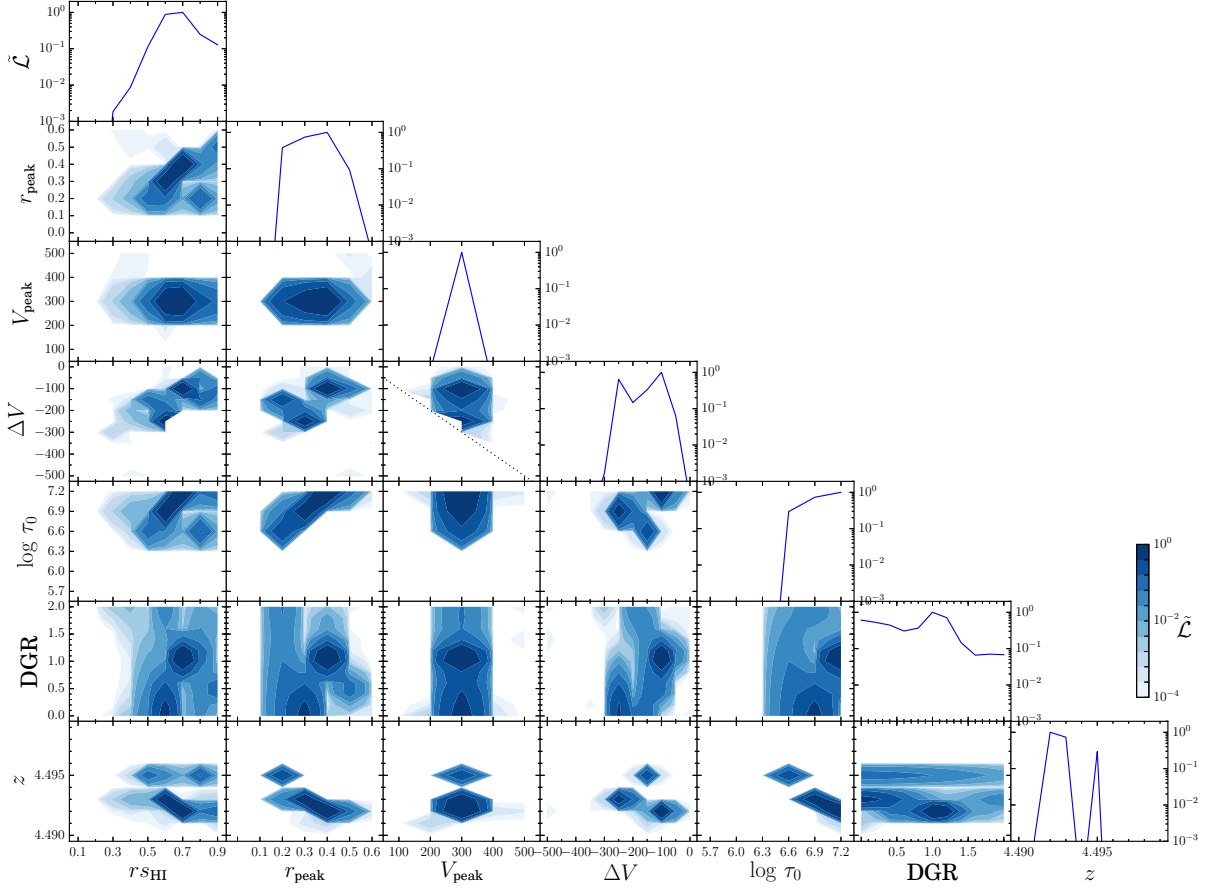


Figure 1. 1D (the top panel of each column) and 2D (the rest) marginal posterior distributions for the spectrum ($\tilde{\mathcal{L}}_{\text{sp}}$) of MUSE #1185. The tilde indicates that posterior values are normalized by their maximum. In the panel of $\Delta V - V_{\text{peak}}$, the dotted line indicates the allowed ΔV range (i.e., $-V_{\text{peak}} < \Delta V < 0$) for a given V_{peak} value to represent decelerated outflowing motion but prevent inflowing motion.

3.1. To Fit Spectra and Surface brightness profiles Separately

Figures 1 and 2 show the posterior distributions of the parameters for the spectrum (\mathcal{L}_{sp}) and surface brightness profile (\mathcal{L}_{SBP}), respectively, of MUSE #1185. Note that posterior values are normalized by their maximum (denoted by $\tilde{\mathcal{L}}$). Overall, spectrum provides tighter constraints on the parameters than surface brightness profile does. Among the seven parameters, redshift is most tightly constrained by spectrum, but neither spectrum nor surface brightness profile constrains DGR. It should be noted that surface brightness profile also provides a constraint on redshift. The results are similar for other targets.

The best-fit parameter sets for spectrum and surface brightness profile, respectively, are found based on their 1D posterior distribution as the maximum posterior location for each parameter. We draw two sets of model spectrum and surface brightness profile (solid line) with observational data (filled circles with error bar) in the left and middle panels: one with the best-fit parameter set for spectrum (Figure 3) and the other with that for surface brightness profile (Figure 4). Each best-fit parameter set reproduces well one, not the other.

The right panels show model profiles of medium density and velocity for each given best-fit parameter set. It is clearly seen that the models for spectrum and surface brightness profile do not necessarily agree with each other; the discrepancy is removed by fitting the spectrum and surface brightness profile simultaneously.

3.2. To Fit Spectra and Surface brightness profiles Simultaneously

To find a best-fit parameter set that explains well both spectrum and surface brightness profile simultaneously, we now explore the total posterior distributions, \mathcal{L}_{tot} , which are given by the product of \mathcal{L}_{sp} and \mathcal{L}_{SBP} . Figure 5 shows those for MUSE #1185 (refer to similar figures in Appendix B for other target galaxies). The total posterior distributions become much sharper than those of spectrum or surface brightness profile. The model spectrum (left)

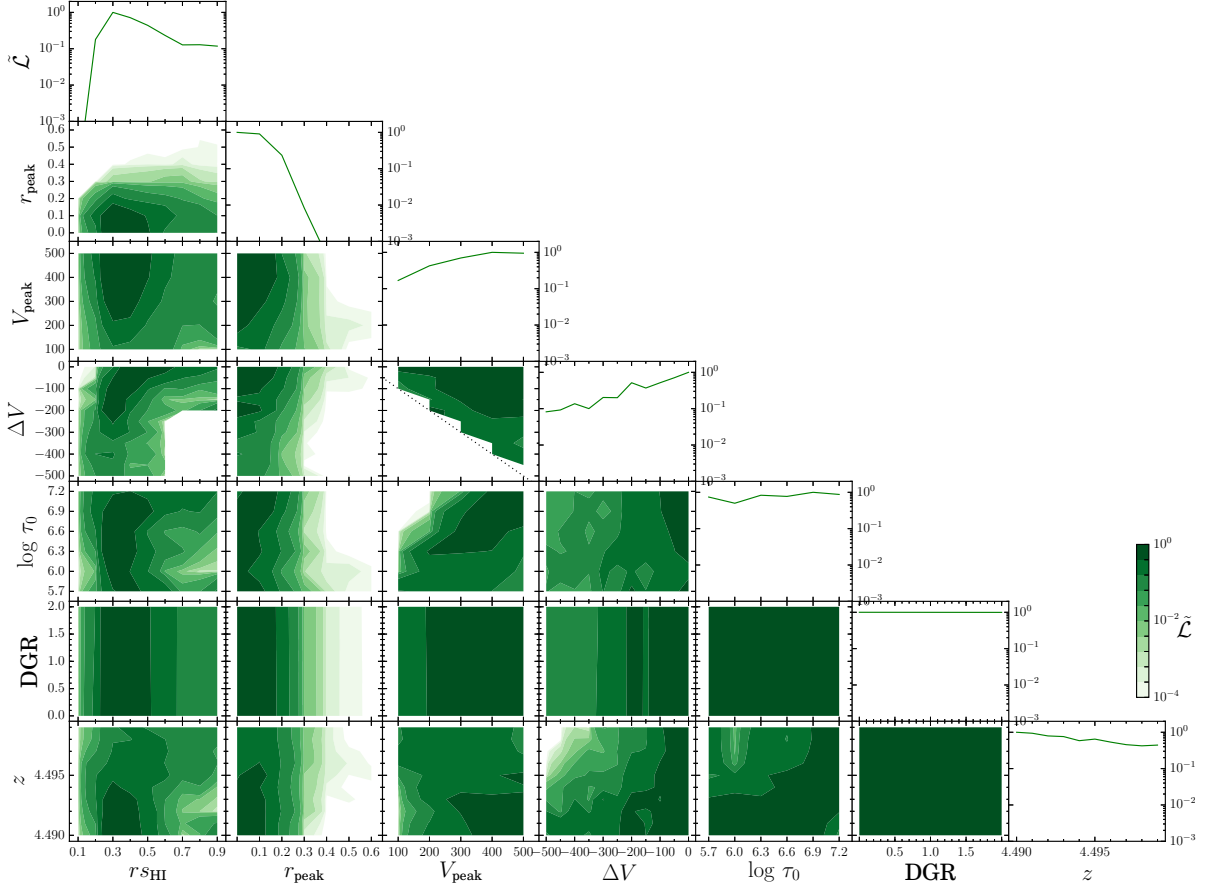


Figure 2. Similar to Figure 1, but (normalized) posterior distributions for the surface brightness profile ($\tilde{\mathcal{L}}_{\text{SBP}}$) of MUSE #1185.

and surface brightness profile (middle) with the best-fit parameter set obtained from \mathcal{L}_{tot} are shown in Figure 6. This parameter set reproduces nicely both the spectrum and surface brightness profile. The model profiles of medium density and velocity obtained from this simultaneous fit are shown in the right panel. The density profile is the same as that obtained from the surface brightness profile fit, while the velocity profile is different from both of the two obtained from the separate fits (see the right panels of Figures 3 and 4). The medium density profile tends to follow that determined by surface brightness profile, as indicated in Table 3 that summarizes fitting results.

We summarize best-fit parameter sets determined by \mathcal{L}_{sp} , \mathcal{L}_{SBP} , and \mathcal{L}_{tot} , respectively, in Table 3 for all the target galaxies. In most cases, the best-fit parameter set determined by \mathcal{L}_{tot} is different from that by either \mathcal{L}_{sp} or \mathcal{L}_{SBP} . In the case of MUSE #53, the parameters are constrained entirely by spectrum, which can be expected from their posterior distributions given by spectrum (Figure 21) that are much sharper than those by surface brightness profile (Figure 22). Although the surface brightness profile does not alter the best-fit parameter values determined by spectrum, it still makes the parameter constraints tighter. This is clearly seen in the total posterior distributions (Figure 23) in comparison with the spectrum posterior distributions (Figure 21).

The constraints of parameters are, of course, largely affected by data quality. The peak values of spectrum and surface brightness profile of MUSE #1185, 82, 6905, and 53 are in the orders of $10^{-18} \text{erg cm}^{-2} \text{s}^{-1} \text{\AA}^{-1}$ and $10^{-17} \text{erg cm}^{-2} \text{s}^{-1} \text{arcsec}^{-2}$, respectively, (refer to filled circles with error bars in Figures 6, 16, 18, and 24) with the mean signal-to-noise ratio ($\langle S/N \rangle \gtrsim 4$) (see the last three columns of Table 2). On the other hand, those of MUSE #1343, 171, 547, and 364 are lower by an order of magnitude with $\langle S/N \rangle \lesssim 4$ (refer to Figures 20, 26, 28, and 30 and Table 2). The posterior distributions for the target galaxies with stronger signals are sharper in general, and therefore parameter constraints are tighter (e.g., Figures 5, 15, 17, 23 versus Figures 19, 25, 27, 29).

Table 3 also shows the reduced chi-square value of the model spectrum ($\chi_{\nu, \text{sp}}^2$) for a given best-fit parameter set. Similarly, the 11th column is that for a model surface brightness profile ($\chi_{\nu, \text{SBP}}^2$). The best-fit parameter set based on \mathcal{L}_{tot} (the last row of each object) gives fairly good reduced chi-square values ($\lesssim 1$) for both spectrum and surface

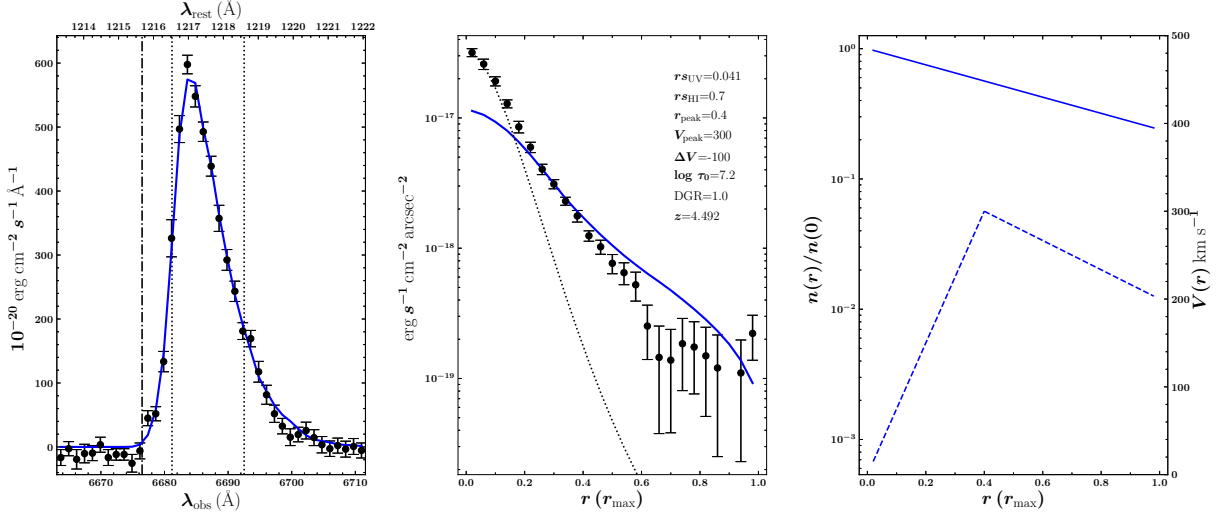


Figure 3. The spectrum (left) and surface brightness profile (middle) are presented: filled circles with error bar are observational data and solid line is the model with the best-fit parameter set for the spectrum of MUSE #1185 (denoted in the upper right of the right panel). In the left panel, two dotted vertical lines denote the wavelength range used for surface brightness profile. The dash-dotted line denotes the Ly α central wavelength in the observer’s frame of the best-fit redshift (lower x-axis) and in the rest frame (upper x-axis, at 1215.67Å). In the middle panel, the dotted line represents the surface brightness profile of the observed UV continuum that is used to reconstruct the spatial distribution of Ly α source, which is an input in our model. In the right panel, the models for density (solid line, y-axis on the left) and velocity (dashed line, y-axis on the right) profiles of medium for the given parameter set are presented.

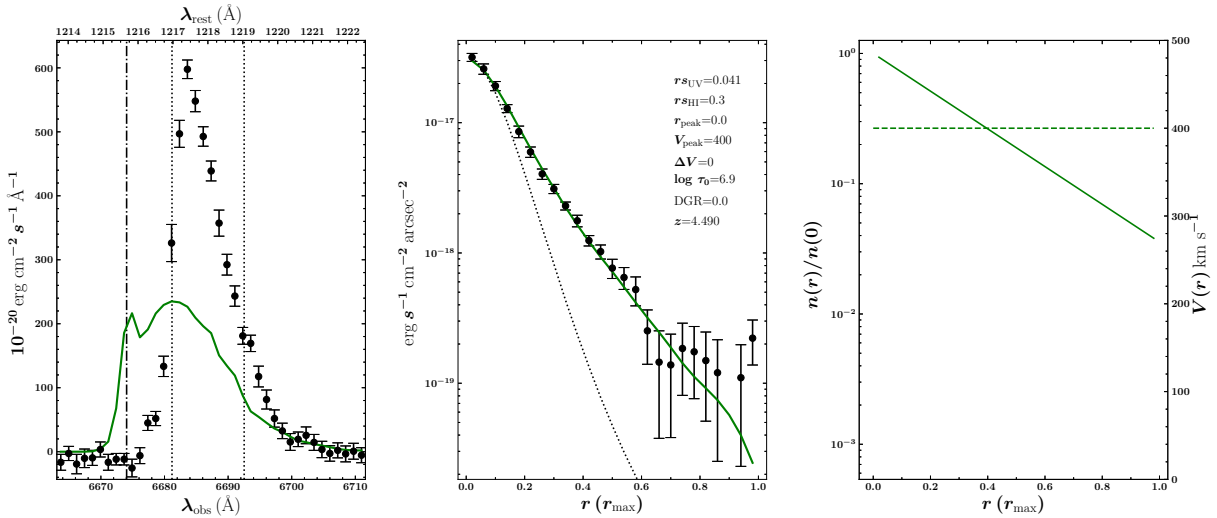


Figure 4. Similar to Figure 3, but with the best-fit model for the surface brightness profile of MUSE # 1185.

brightness profile, which quantitatively shows that the model successfully fits the observation.

4. DISCUSSION

4.1. Interpretations on Best-fit Results

In this section, we compare the best-fit values of some of our model parameters such as V_{peak} and τ_0 with those from other studies. Garel et al. (2012) constructed high-redshift LAEs in a dark matter-only cosmological simulation by implementing a semi-analytic model with an expanding shell model. Their model galaxies, which are tuned to give a good match to observed UV and Ly α luminosity functions, have the expanding velocity of $\sim 150\text{--}200 \text{ km s}^{-1}$

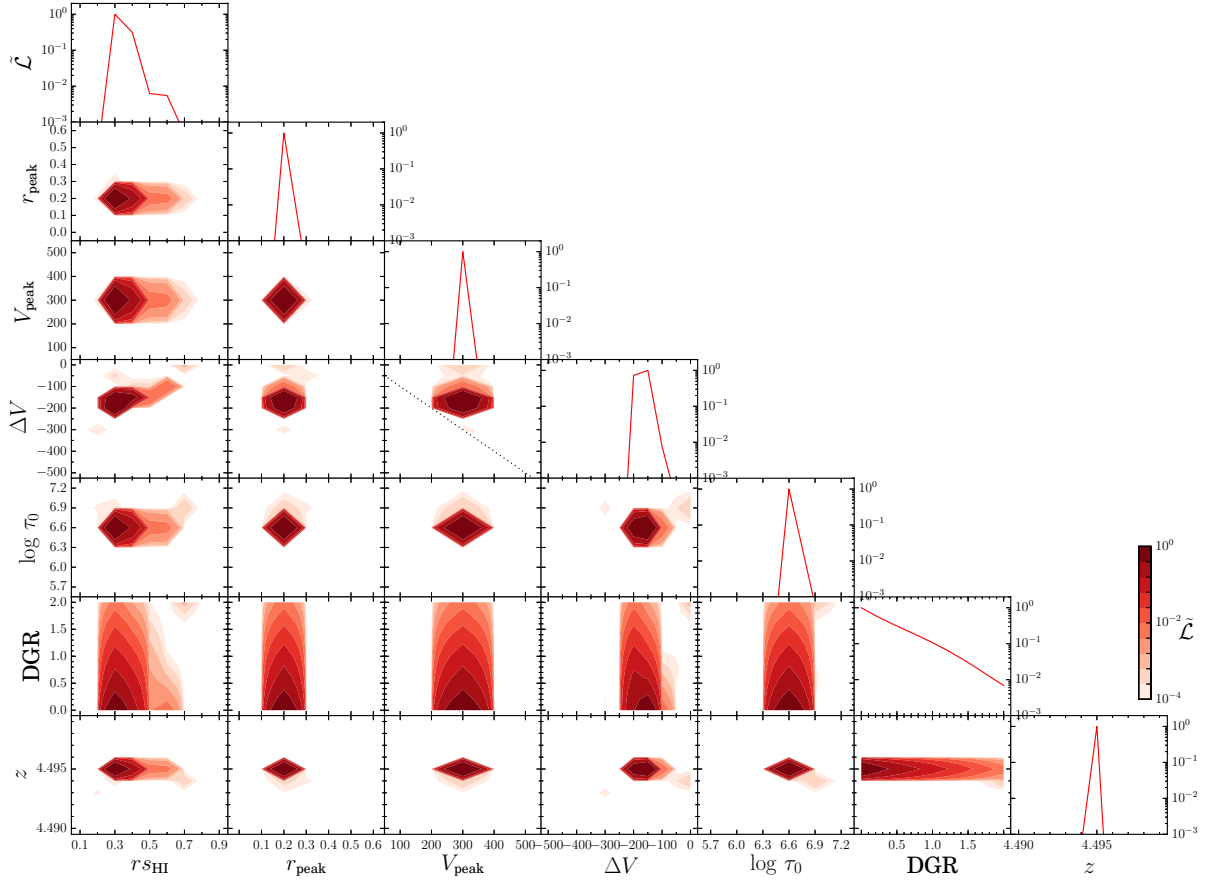


Figure 5. Similar to Figure 1, but for total posterior distributions ($\tilde{\mathcal{L}}_{\text{tot}}$) of MUSE #1185.

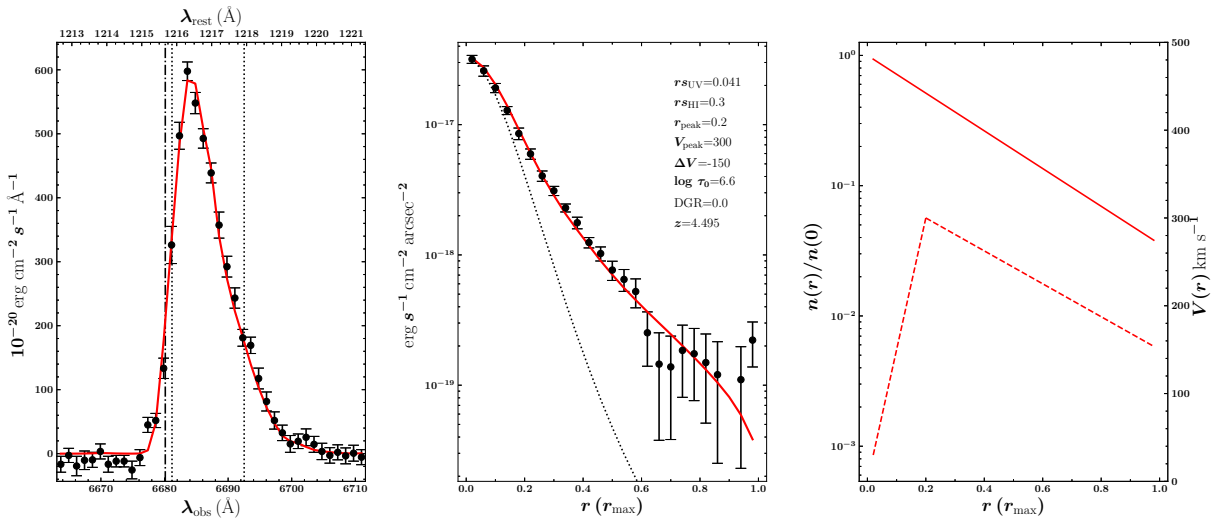


Figure 6. Similar to Figure 3, but with the best-fit model obtained by considering both spectrum and surface brightness profile of MUSE #1185.

Table 3. Best-fit Parameter Values

MUSE #	\mathcal{L}^a	$r_{\text{SH I}}$	r_{peak}	V_{peak}	ΔV	$\log \tau_0$	DGR	z	$\chi^2_{\nu, \text{sp}}^b$	$\chi^2_{\nu, \text{SBP}}^c$
1185	sp	$0.7_{-0.1}^{+0.2}$	$0.4_{-0.1}^{+0.2}$	300_{-43}^{+43}	-100_{-104}^{+100}	$7.2_{-0.6}$	$1.0_{-0.6}^{+0.8}$	$4.492_{-0.002}^{+0.001}$	1.21	16.18
	SBP	$0.3_{-0.2}^{+0.2}$	$0.0_{-0.1}^{+0.1}$	400_{-148}^{+100}	0_{-238}	$6.9_{-0.7}$	$0.0_{-0.7}^{+1.4}$	$4.490_{-0.001}^{+0.005}$	120.48	0.84
	tot	$0.3_{-0.1}^{+0.1}$	$0.2_{-0.0}^{+0.0}$	300_{-43}^{+43}	-150_{-37}^{+150}	$6.6_{-0.1}$	$0.0_{-0.1}^{+0.4}$	$4.495_{-0.000}^{+0.000}$	1.88	1.14
82	sp	$0.9_{-0.5}$	$0.2_{-0.1}^{+0.1}$	300_{-82}^{+200}	0_{-297}	$7.2_{-0.6}$	$0.0_{-0.6}^{+1.2}$	$3.602_{-0.006}^{+0.001}$	3.70	5.21
	SBP	$0.7_{-0.2}^{+0.2}$	$0.0_{-0.1}^{+0.1}$	500_{-277}	-200_{-300}^{+97}	$5.7_{-0.5}$	$0.0_{-0.5}^{+1.4}$	$3.601_{-0.003}^{+0.003}$	44.19	10.41
	tot	$0.5_{-0.1}^{+0.4}$	$0.1_{-0.0}^{+0.0}$	300_{-43}^{+43}	-250_{-30}^{+47}	$6.6_{-0.1}$	$2.0_{-1.3}$	$3.604_{-0.000}^{+0.000}$	0.94	1.16
6905	sp	$0.5_{-0.3}^{+0.3}$	$0.2_{-0.2}^{+0.2}$	200_{-62}^{+55}	-150_{-108}^{+108}	$7.2_{-0.6}$	$1.0_{-0.7}^{+0.7}$	$3.096_{-0.001}^{+0.001}$	5.05	20.58
	SBP	$0.3_{-0.2}^{+0.3}$	$0.0_{-0.2}^{+0.2}$	500_{-253}	-100_{-139}^{+100}	$6.0_{-0.3}$	$2.0_{-1.4}$	$3.098_{-0.005}^{+0.002}$	48.80	0.38
	tot	$0.1_{-0.1}^{+0.0}$	$0.0_{-0.1}^{+0.1}$	300_{-53}^{+52}	-300_{-83}^{+44}	$6.3_{-0.6}^{+0.3}$	$0.0_{-0.6}^{+1.3}$	$3.098_{-0.001}^{+0.001}$	0.82	0.49
1343	sp	$0.1_{-0.2}^{+0.5}$	$0.4_{-0.2}^{+0.2}$	500_{-286}	0_{-264}	$7.2_{-0.7}$	$1.4_{-0.8}^{+0.7}$	$3.964_{-0.004}^{+0.002}$	0.17	1.51
	SBP	$0.9_{-0.4}$	$0.3_{-0.2}^{+0.2}$	400_{-164}^{+100}	-200_{-168}^{+141}	$7.2_{-1.0}$	$1.0_{-0.7}^{+0.7}$	$3.963_{-0.003}^{+0.003}$	1.02	0.34
	tot	$0.8_{-0.3}^{+0.1}$	$0.4_{-0.2}^{+0.2}$	200_{-100}^{+168}	-200_{-167}^{+125}	$6.9_{-0.4}^{+0.3}$	$2.0_{-1.4}$	$3.964_{-0.004}^{+0.002}$	0.96	1.36
53	sp	$0.4_{-0.0}^{+0.0}$	$0.1_{-0.0}^{+0.0}$	300_{-43}^{+43}	-50_{-18}^{+18}	$6.3_{-0.1}^{+0.1}$	$2.0_{-1.0}$	$4.776_{-0.000}^{+0.000}$	1.65	1.50
	SBP	$0.2_{-0.1}^{+0.2}$	$0.1_{-0.1}^{+0.1}$	500_{-253}	0_{-227}	$6.0_{-0.3}^{+0.6}$	$0.0_{-0.3}^{+1.4}$	$4.775_{-0.003}^{+0.002}$	117.90	6.84
	tot	$0.4_{-0.1}^{+0.1}$	$0.1_{-0.1}^{+0.0}$	300_{-43}^{+43}	-50_{-23}^{+22}	$6.3_{-0.1}^{+0.1}$	$2.0_{-1.0}$	$4.776_{-0.000}^{+0.000}$	1.65	1.50
171	sp	$0.1_{-0.1}^{+0.4}$	$0.6_{-0.4}$	200_{-100}^{+191}	-100_{-108}^{+100}	$7.2_{-0.7}$	$2.0_{-1.4}$	$3.880_{-0.001}^{+0.002}$	2.24	6.86
	SBP	$0.5_{-0.2}^{+0.3}$	$0.0_{-0.1}^{+0.1}$	500_{-259}	-200_{-205}^{+117}	$6.6_{-0.6}^{+0.5}$	$2.0_{-1.4}$	$3.881_{-0.002}^{+0.004}$	10.22	0.79
	tot	$0.8_{-0.4}^{+0.1}$	$0.0_{-0.1}^{+0.1}$	200_{-51}^{+48}	0_{-175}	$6.3_{-0.2}^{+0.2}$	$2.0_{-1.4}$	$3.882_{-0.001}^{+0.003}$	1.20	0.81
547	sp	$0.9_{-0.5}$	$0.2_{-0.2}^{+0.2}$	200_{-100}^{+219}	-150_{-254}^{+84}	$6.6_{-0.2}^{+0.7}$	$0.0_{-0.2}^{+1.4}$	$5.973_{-0.001}^{+0.002}$	13.46	12.09
	SBP	$0.5_{-0.1}^{+0.2}$	$0.1_{-0.1}^{+0.1}$	500_{-225}	-500_{-137}^{+137}	$5.7_{-0.5}$	$0.0_{-0.5}^{+1.4}$	$5.978_{-0.005}^{+0.001}$	39.42	1.30
	tot	$0.7_{-0.2}^{+0.2}$	$0.1_{-0.1}^{+0.1}$	300_{-78}^{+200}	-200_{-188}^{+88}	$6.3_{-0.1}^{+1.0}$	$2.0_{-1.4}$	$5.974_{-0.001}^{+0.001}$	1.25	1.07
364	sp	$0.5_{-0.2}^{+0.3}$	$0.1_{-0.1}^{+0.4}$	500_{-236}	0_{-231}	$6.3_{-0.5}^{+0.3}$	$2.0_{-1.4}$	$3.939_{-0.001}^{+0.001}$	1.81	3.42
	SBP	$0.5_{-0.2}^{+0.2}$	$0.0_{-0.2}^{+0.2}$	400_{-167}^{+100}	-200_{-174}^{+108}	$6.6_{-0.6}^{+0.5}$	$0.0_{-0.6}^{+1.4}$	$3.935_{-0.001}^{+0.004}$	3.55	0.64
	tot	$0.9_{-0.4}$	$0.3_{-0.1}^{+0.4}$	200_{-70}^{+77}	-200_{-300}^{+67}	$6.0_{-0.3}^{+0.3}$	$2.0_{-1.4}$	$3.939_{-0.001}^{+0.004}$	0.68	0.36

NOTE—Note that $r_{\text{SH I}}$ and r_{peak} are in the normalized unit by r_{max} , and DGR is in the unit of the value of the Milky Way (DGR_{MW}).

^aThe marginal posterior distribution of parameters that is used to determine a given best-fit parameter set among those obtained using spectrum (\mathcal{L}_{sp}), surface brightness profile (\mathcal{L}_{SBP}), and both (\mathcal{L}_{tot}).

^bThe reduced chi-square value of the model spectrum with a given best-fit parameter set (of a given row in the table).

^cThe reduced chi-square value of the model surface brightness profile with a given best-fit parameter set.

and H I column density of $\sim 10^{20} \text{ cm}^{-2}$. We also compare our results with those of Verhamme et al. (2008) and Yang et al. (2016). Verhamme et al. (2008) reproduced the observed Ly α spectra of 11 high-redshift ($z \sim 3$) Lyman break galaxies using an expanding shell model, and they found the best models for these galaxies with the expanding velocity of $\sim 150\text{--}200 \text{ km s}^{-1}$ and H I column density of $\sim 2 \times 10^{19}\text{--}7 \times 10^{20} \text{ cm}^{-2}$. Yang et al. (2016) modeled 12 low-redshift ($z \sim 0.2$) green pea galaxies⁴ as an expanding shell, too. Their best models for these galaxies give the expanding velocity of $\sim 30\text{--}350 \text{ km s}^{-1}$ and H I column density of $\sim 10^{19}\text{--}10^{20} \text{ cm}^{-2}$. All these results are similar to our results.

There are other estimates on the kinematics of medium in galaxies using interstellar/circumgalactic absorption lines. Steidel et al. (2010) measured absorption lines in QSO spectra made by circumgalactic gas of star-forming galaxies at redshift $2 \lesssim z \lesssim 3$ that are on the sightlines to the QSOs. They then examined properties of absorption lines as a function of the galactocentric impact parameter up to $\gtrsim 100 \text{ kpc}$, and modeled them using outflowing halos with constant/decelerating velocity profiles and a covering factor profile. A constant velocity profile gives an outflowing velocity of $650\text{--}820 \text{ km s}^{-1}$, and a decelerating velocity profile gives a mean outflowing velocity of $\sim 200\text{--}300 \text{ km s}^{-1}$. We could not directly compare because of different assumptions, but the estimate with a constant velocity profile is larger than our best-fit values and the estimate with a decelerating velocity profile is more or less similar to ours. Because the estimate of the outflowing velocity varies largely depending on which velocity profile is used, the disagreement between these estimates could be not an issue. It should be also noted that the best-fit velocity varies depending on the choice of a covering factor profile, and possibly other factors such as optical depth. Moreover, different emission/absorption lines

⁴ Green pea galaxies are nearby compact starburst galaxies and are thought to be analogous to high-redshift star-forming galaxies.

trace different kinds of gas, thus different kinematics. Therefore, these suggest that our constraints on the outflowing velocity are consistent with previous studies in general.

The last thing we would like to address is the constraint on redshift. We set redshift as a free parameter, and find its best-fit values to have shifts of 0.001–0.008 to lower redshifts than the estimates when the peak of Ly α spectrum is assumed to be at the rest-frame Ly α central wavelength. This means that Ly α line is more redshifted than that by the systemic redshift of galaxies, which is due to the resonance scattering of Ly α . Compared to the typical redshift error of Sloan Digital Sky Survey (i.e., 30 km s⁻¹, [Strauss et al. 2002](#)), the shifts of 0.001–0.008 are non-negligible. More importantly, the accuracy of redshift estimate is transferred to that of the estimates on τ_0 and subsequently other parameters. Reminding that Ly α -based redshift estimates are not always correct (e.g., [Orlitová et al. 2018](#)), it is necessary to secure other reliable estimates of redshift if available.

4.2. Advantages of Using Both Spectrum and Surface Brightness Profile

We examine the degeneracy between parameters based on the 2D posterior distributions (e.g., see [Figures 1 and 2](#)). In the case of spectrum, degeneracies of τ_0 – r_{peak} and z – τ_0 appear prominently and commonly for all the target galaxies. A weak degeneracy between z and r_{peak} also appears in the majority of the target galaxies. The posterior distributions of surface brightness profile also show degeneracies of ΔV – $r_{s_{\text{HI}}}$, τ_0 – V_{peak} , z – V_{peak} , and z – τ_0 for most target galaxies, which are overall less prominent than those of spectrum. Interestingly, the degeneracy between z and τ_0 appears to be opposite for spectrum (negative correlation) and surface brightness profile (positive). Although parameter degeneracy itself hinders precise parameter constraints, such opposite behaviors of parameter degeneracy for spectrum and surface brightness profile together can provide tighter constraints on z , τ_0 , and consequently on other parameters as well.

The opposite behaviors of parameter degeneracy is partly attributed to the fact that the posterior distributions of spectrum and surface brightness profile prefer different parts of parameter spaces. This results in quite different best-fit parameter sets for spectrum and surface brightness profile as summarized in [Table 3](#). The difference is non-negligible as seen in [Figures 3 and 4](#); the best-fit parameter for one of spectrum and surface brightness profile completely fails at reproducing the other. The comparison between the $\chi^2_{\nu, \text{SP}}$ and the $\chi^2_{\nu, \text{SBP}}$ with the best-fit parameter set for either spectrum or surface brightness profile shows this failure in a quantitative way. The difference (i.e., ratio) between these two chi-squares can be as large as by a factor of a hundred. This indicates that spectrum and surface brightness profile are complementary and orthogonal in constraining our model parameters. Therefore, these two observables together can a lot better constrain parameters, which is shown in the previous section with the total posterior distributions that become much sharper than those of spectrum or surface brightness profile. Even the redshift constraint, which is expected to be done primarily by spectrum, is affected when surface brightness profile is taken into account. This constraining power of surface brightness profile on redshift comes from the restriction on wavelength range for surface brightness profile (i.e., image bandwidth). In the cases of MUSE #1343, 53, and 364, surface brightness profile does not alter the redshift constraint by spectrum. However, surface brightness profile still contributes to the parameter constraint by making it tighter, as seen in the total posterior distribution for redshift compared to its spectrum posterior distribution (e.g., [Figure 23](#) versus [Figure 21](#)).

4.3. Ly α Spectrum and Surface Brightness Profile Variation in Model Parameter Space

We explore the variations of Ly α spectrum and of surface brightness profile in the model parameter space to better understand the fitting results and the parameter degeneracy in the previous sections. Here, we have convolved raw model spectrum and surface brightness profile with a Gaussian kernel and a Moffat kernel, respectively, as described in [Section 2.3](#). However, we have applied neither the size of aperture (to spectrum) nor the image bandwidth (to surface brightness profile) to first understand pure impacts of the physical parameters. The effect of the aperture size will be indirectly discussed later in [Section 4.6](#) with spatially resolved spectra. We examine the impacts of six parameters except redshift. The results for τ_0 and $r_{s_{\text{HI}}}$ are described in detail here, but those for other parameters are presented in [Appendix C](#). It should be noted that we explore the impacts of parameters on the *shapes* of spectrum and surface brightness profile.

Although Ly α radiative transfer process is a bunch of random scattering events, we can roughly guess the shapes of emerging Ly α spectrum and surface brightness profile by inferring the frequency change and the last scattering position of photons, respectively. The rule of thumb is that the larger the *effective* optical-depth⁵ is, the larger the frequency change is. A larger frequency change results in a broader spectrum with its peak farther away from the Ly α central

⁵ Conventionally optical depth refers to the cumulative optical depth that is measured at a fixed frequency. The *effective* optical-depth refers to an optical depth that takes into account the frequency change (thus the change of cross section) of photons, due to the relative motion between the photons and the medium, in the rest frame of the medium.

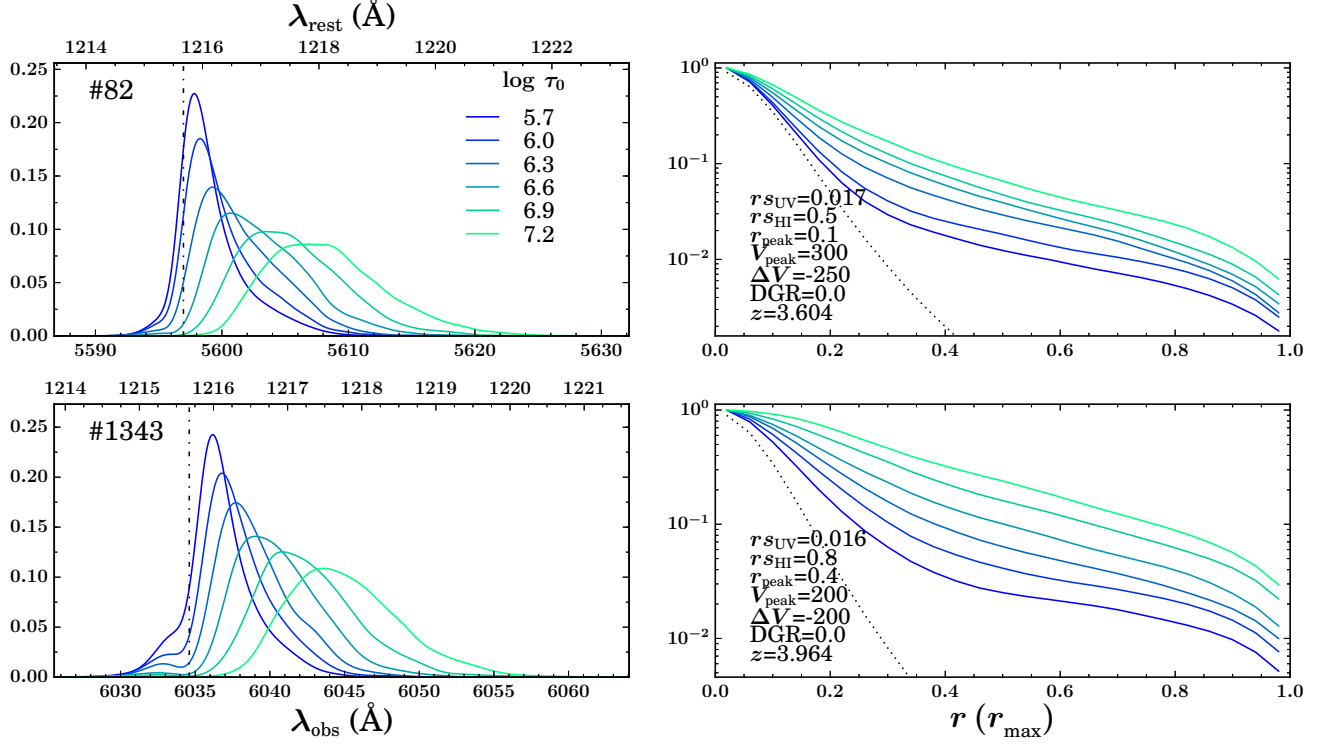


Figure 7. Spectra (left panel) and surface brightness profiles (right panel) with varying τ_0 for two of our target galaxies. The MUSE id of the chosen galaxies is written in top left of each spectrum panel. The parameters other than τ_0 are fixed at their best-fit values except DGR that is fixed at zero. The dot-dashed line in the spectrum panels represents the Ly α central wavelength, 1215.67Å, and the dotted line in the surface brightness profile panels represents the surface brightness profile of UV continuum (i.e., Ly α source distribution).

wavelength, from which the correlation between peak shift and FWHM is naturally expected, as discussed in Section 4.5. The last scattering position can be guessed by inferring the location where the cumulative effective optical-depth reaches a certain value. We try to understand the impact of each parameter on Ly α spectrum and surface brightness profile based on this rule of thumb. However, it should be noted that the details of the impact of each parameter can manifest differently depending on the values of other parameters.

We show changes in the Ly α spectrum and surface brightness profile with each parameter. We choose two galaxies for which the impact of a parameter on the spectrum and surface brightness profile is apparent most significantly. Our choice can differ depending on a parameter of interest. For illustration, we fix parameters other than the one under consideration at their best-fit values. However, DGR is fixed at zero unless it is the parameter of interest (i.e., Figure 34) to make problems simpler. Spectrum is normalized by its total intensity, and surface brightness profile is normalized by its maximum value (i.e., the value at $r = 0$) for convenience.

We start from the changes of spectrum and surface brightness profile with τ_0 , which is easy to understand. Figure 7 shows the cases of MUSE #82 and 1343. The peak of spectrum moves farther away from the central wavelength and the width becomes broader as τ_0 increases. A surface brightness profile becomes flatter with increasing τ_0 . These trends are because the number of scatterings in general increases accordingly.

Figure 8 shows the changes of Ly α spectrum and surface brightness profile with $r_{S_{\text{HI}}}$ for the same galaxies. Spectrum does not change significantly with $r_{S_{\text{HI}}}$, but surface brightness profile becomes clearly flatter as $r_{S_{\text{HI}}}$ increases. In a less centrally-concentrated medium (larger $r_{S_{\text{HI}}}$), Ly α photons can diffuse out of the central region more easily. In turn, last scatterings tend to happen at larger radii, which results in a flatter surface brightness profile. Meanwhile, it is not obvious to understand the behavior of spectral shape with $r_{S_{\text{HI}}}$. Although the column density remains the same, redistributing matter can either effectively increase or decrease optical depth depending on the velocity structure of the medium. It is not only effective optical-depth but also last scattering positions that change with $r_{S_{\text{HI}}}$, which means that the velocities at which Ly α photons are scattered off also change. All of these factors together make the

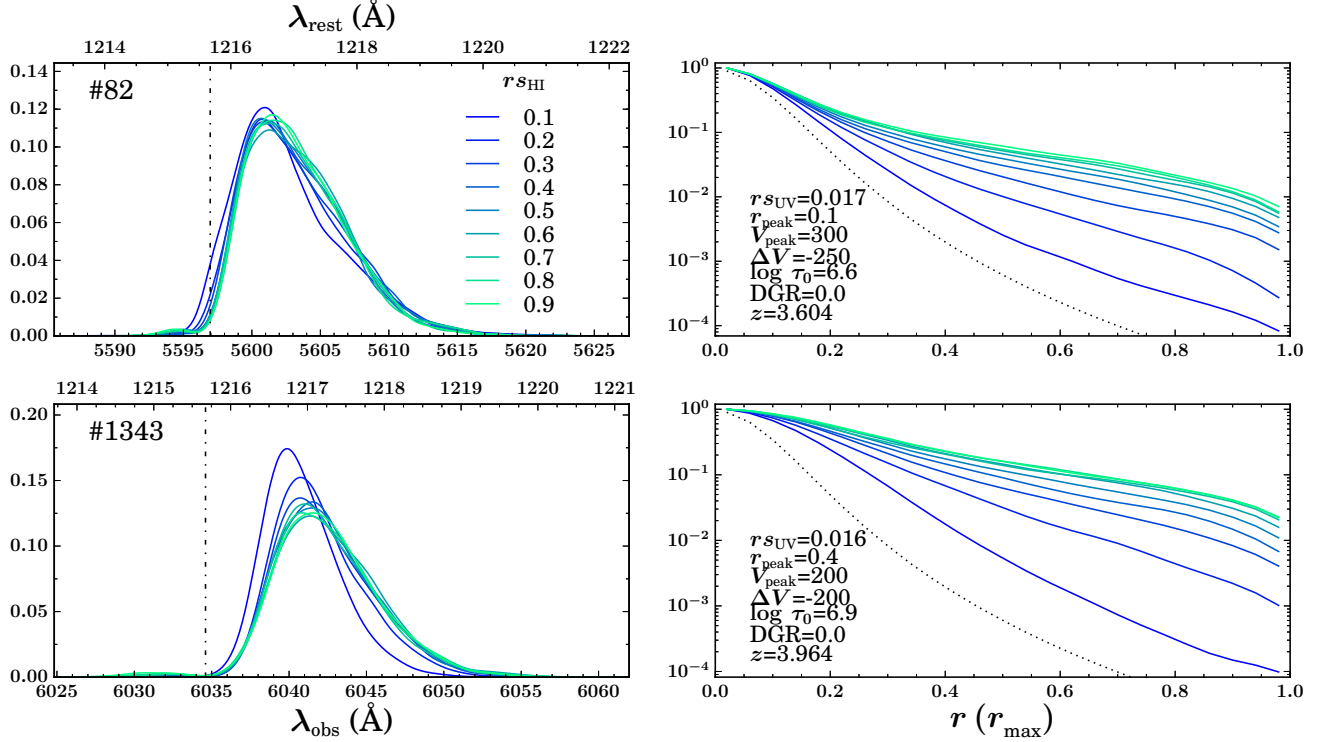


Figure 8. Similar to Figure 7, but with varying rs_{HI} .

prediction on the change of spectral shape with rs_{HI} more complicated.

There are two competing factors playing roles in forming the spectral shape in an expanding medium: (1) the Doppler frequency shift and (2) the effective optical-depth. In an expanding medium, the frequency of a photon being scattered would be Doppler-shifted when transformed from the fixed frame to the medium frame; as a result, the final photon frequency after many scatterings will be shifted by an amount proportional to the expanding velocity. Therefore, the frequency changes due to the Doppler effect (if photons undergo enough number of scatterings) will be more significant in a faster medium than in a slower medium. However, as the medium's velocity increases, the effective optical-depth would decrease, and thus the number of scatterings the photons undergo before escaping the medium will decrease as well; consequently, we expect that a faster medium yields a smaller frequency change. This latter effect will be particularly significant in a fast-moving medium. We found, as shown in Appendix D, that the frequency shift due to the Doppler effect in an expanding medium is essential in a relatively slow-moving medium; however, the effective optical-depth becomes more critical in a fast-moving medium.

For example, if the medium velocity is largely decelerated at large radii, putting more matter at larger radii (i.e., larger rs_{HI}) will result in a larger effective optical-depth. Therefore, as seen for surface brightness profiles in Figure 8, more scatterings tend to happen at larger radii, thus by medium at smaller velocities. However, this does not make spectrum necessarily broader and its peak farther away from the central wavelength. The two competing effects (the Doppler frequency shift and the effective optical-depth) seem to be canceled out in the case of MUSE #82, while the latter effect (i.e., enhanced effective optical-depth by increasing rs_{HI}) overwhelms the former effect (i.e., smaller frequency shift due to smaller medium velocity) in the case of MUSE #1343. The impact of rs_{HI} on spectrum could be more significant when there is non-negligible amount of Ly α photons emitted at large radii (i.e., larger rs_{cont}). Indeed, all of our target galaxies are modeled to have a very compact Ly α source distribution as inferred from their UV distribution (see Table 2), which could limit the impact of rs_{HI} on spectrum.

As r_{peak} decreases, spectrum becomes broader with higher intensities at the central wavelength and at the red wing, and surface brightness profile tends to be steeper at inner radii (Figure 31). Increasing V_{peak} has an effect similar to but stronger than that of decreasing r_{peak} ; spectrum shows a much clearer peak shift toward the central wavelength and surface brightness profile becomes steeper over the entire range (Figure 32). Here, we need to note the V_{peak} in Figure 32 is similar to the high velocities considered in Appendix D, for which no considerable scatterings happen and

thus the Doppler frequency shift effect is insignificant. As ΔV decreases (i.e., the edge velocity decreases), surface brightness profile becomes flatter, and spectrum has lower intensity at the central wavelength with its peak shift toward the red side (Figure 33). When the edge velocity becomes zero, the emergent spectrum shows a small blue bump. The spectrum becomes slightly sharper and its peak comes closer to the central wavelength as DGR increases; the impact of DGR appears more apparent when optical depth is larger, as shown in the bottom row of Figure 34. The impact of DGR on surface brightness profile is in general minor. Please refer to Appendix C for the interpretations on these behaviors.

Multiple parameters show impacts on spectrum or surface brightness profile. Therefore, a degeneracy between parameters is naturally expected, and we mentioned some of them in the 2D posterior distributions of Section 4.2. We now can understand these degeneracies in a qualitative way from the spectral and surface brightness profile variations in the parameter space examined above. The most obvious degeneracy is found to be the one for τ_0 and z in spectrum. It is because their impacts on spectrum are strong enough to manifest themselves consistently for any combinations of other parameters. A redshift z stretches a wavelength range by a factor of $(1+z)$. Thus, both τ_0 and z cause a larger shift of the peak and a broader width when their value increases. This leads to the negative degeneracy between τ_0 and z as noted in Section 4.2. Meanwhile, r_{peak} and V_{peak} also have impacts on the spectral shape, but their impacts are not as significant as those of τ_0 and z . Moreover, the changes of the peak shift and the width with r_{peak} or V_{peak} do not appear consistently for all cases; sometimes a larger shift comes with a broader width and sometimes not. Therefore, a degeneracy involved with r_{peak} or V_{peak} could be either strong or weak. The parameter degeneracy in the surface brightness profile is weak as in Figure 2. This is not because parameters play unique roles in shaping surface brightness profile, but because their roles are too simple. Although most parameters have a clear impact on the surface brightness profile, the variation of surface brightness profile made by each parameter is mostly about the change in the steepness. Such a simple variation is not enough to discriminate the effects of different parameters, which leads to poor parameter constraints from surface brightness profile. Still, we can better constrain parameters using both spectrum and surface brightness profile as seen in the posterior distributions of \mathcal{L}_{tot} sharper than those of \mathcal{L}_{sp} or \mathcal{L}_{SBP} (e.g., Figure 5 versus Figures 1 or 2). This can be understood from the fact that the variations of spectrum and surface brightness profile with parameters are quite diverse. Some parameters change only one of the two, while others change both (e.g., rs_{HI} versus r_{peak}); some parameters change the spectrum in a way similar to other parameters, but not the surface brightness profile (e.g., τ_0 versus z). Such different behaviors make total posterior distributions tighter and break parameter degeneracy.

4.4. Spatial Extent of Ly α Halos and Its Dependence on Model Parameters

One notable feature of Ly α halos around high- z star-forming galaxies is their size that is typically much larger than the size observed in the UV continuum. The ratio of the scale radii of the brightness distributions in Ly α and UV continuum ($rs_{\text{halo}}/rs_{\text{cont}}$) of our target galaxies covers a wide range from 3.5 to 21, with a mean value of 10.2. Indeed, our target galaxies have a size much larger in Ly α than in UV continuum. We perform a simple analysis to examine correlations between each model parameter and $rs_{\text{halo}}/rs_{\text{cont}}$ for a hint on which physical parameter is responsible for the property of the extended Ly α halos.

Figure 9 shows the correlations between $rs_{\text{halo}}/rs_{\text{cont}}$ and each of six parameters that are $rs_{\text{HI}}/rs_{\text{cont}}$, $r_{\text{peak}}/rs_{\text{cont}}$, $V_{\text{peak}}/r_{\text{peak}}$, ΔV , V_{edge} , and τ_0 for our target galaxies (see filled circles with error bars in each panel). We exclude DGR and z because they are certainly not responsible for the extent of Ly α emission. Errors are calculated from the likelihood distributions of model parameters, as summarized in Table 3. Although the errors are asymmetric, we assume symmetric errors by taking the mean of lower and upper errors when we need to apply the error propagation for the final error estimation (except ΔV and τ_0). In any case, the error estimation is rough, and thus it should not be taken at face value. Among the model parameters, $rs_{\text{HI}}/rs_{\text{cont}}$ and $r_{\text{peak}}/rs_{\text{cont}}$ show non-negligible correlations with $rs_{\text{halo}}/rs_{\text{cont}}$ (p -value smaller than 0.1), and their Spearman rank-order correlation coefficients are 0.74 and 0.64, respectively. These correlations suggest that the large extent of Ly α emission results from wide distribution of neutral hydrogen medium and from slow increase of outflowing velocity in the inner region. Another correlation that might be worth paying attention to is the one between $rs_{\text{halo}}/rs_{\text{cont}}$ and V_{edge} (Spearman rank-order correlation coefficient is -0.61 and p -value is 0.11), which indicates that Ly α emission is more extended when the velocity of outer medium is smaller (i.e., the velocity decrease in the outer region is larger). This is because more Ly α photons, especially those that freely escape from the inner region, can be scattered and escape at large radii, which results in more Ly α emission at large radii and thus a larger extent of Ly α halos.

To summarize, large spatial extents of Ly α halos seem relevant to large spatial extents of UV emission (a result of L17) and neutral hydrogen medium, and small bulk velocities of the medium at small and large radii. This needs to

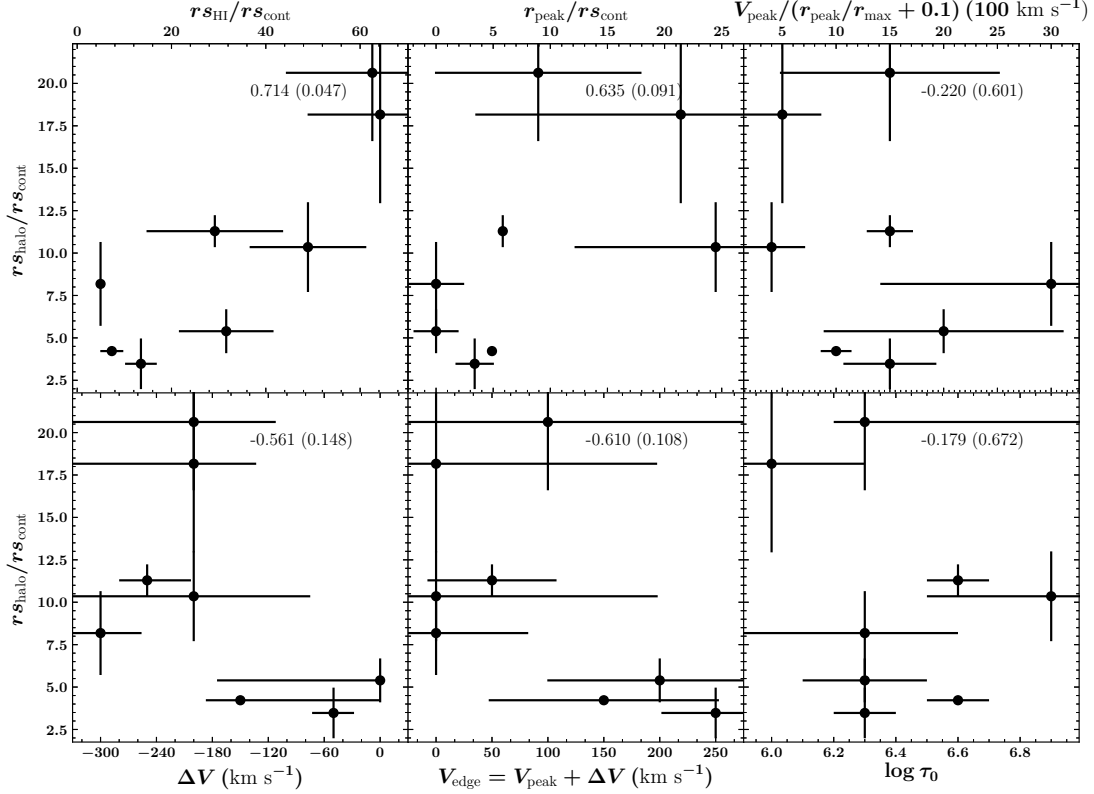


Figure 9. Correlation between r_{shalo}/r_{scont} and each of six parameter values of r_{sHI} , r_{peak} , V_{peak}/r_{peak} , ΔV , $V_{edge} (= V_{peak} + \Delta V)$, and τ_0 of our eight target galaxies. The Spearman rank-order correlation coefficient and p -value of each correlation are given in the top right of each panel (one in the parenthesis is p -value). In the top left panel for r_{scont} , all galaxies in L17 are also presented with open gray circles and their Spearman rank-order correlation coefficient and p -value are also written in gray.

be further examined using a larger galaxy sample in future studies.

4.5. Correlation between Peak Shift and FWHM of Ly α Spectrum

The correlation between peak shift and FWHM of Ly α spectrum is naturally expected from the resonant scattering process of Ly α photons. This correlation has been recognized as a way to derive a correct systemic redshift of a galaxy when only the Ly α emission line is available (e.g. Zheng & Wallace 2014). Recently, Verhamme et al. (2018) found an empirical relation between red peak shift and FWHM using 45 galaxies for which lines other than Ly α line can be used for the systemic redshift estimate. They showed that this relation recovers the systemic redshift estimate with an accuracy of $\leq 100 \text{ km s}^{-1}$.

We also confirm this correlation using all of our 13,230 simulations (blue density contours in Figure 10). However, the distribution of peak shifts and FWHMs of our simulated spectra has an offset from the empirical relation found by Verhamme et al. (2018, red line). Verhamme et al. (2018) compared in their Figure 4 the correlation from observations with that from models such as expanding shells, spheres or bi-conical outflows (Schaerer et al. 2011; Zheng & Wallace 2014); there also exists an offset between the two, which is however in the opposite direction of ours. This implies that the correlation between peak shift and FWHM can be a model discriminator.

We explore correlations between model parameters and peak shift (top) or FWHM (bottom) in Figure 11. Both peak shift and FWHM show strong correlations with optical depth (rightmost panel in each row), which is the main driver of the correlation between peak shift and FWHM in Figure 10. While their correlations with other parameters are relatively weak, the correlation with velocity profile parameters appears interesting (middle panels); for example, a peak shift is negatively correlated with medium velocity, and FWHM, on the contrary, is positively correlated. The negative correlation between peak shift and medium velocity is because Ly α photons tend to experience less scatterings when medium velocity is larger (the medium velocity in our model is relatively large, and thus the effect of effective

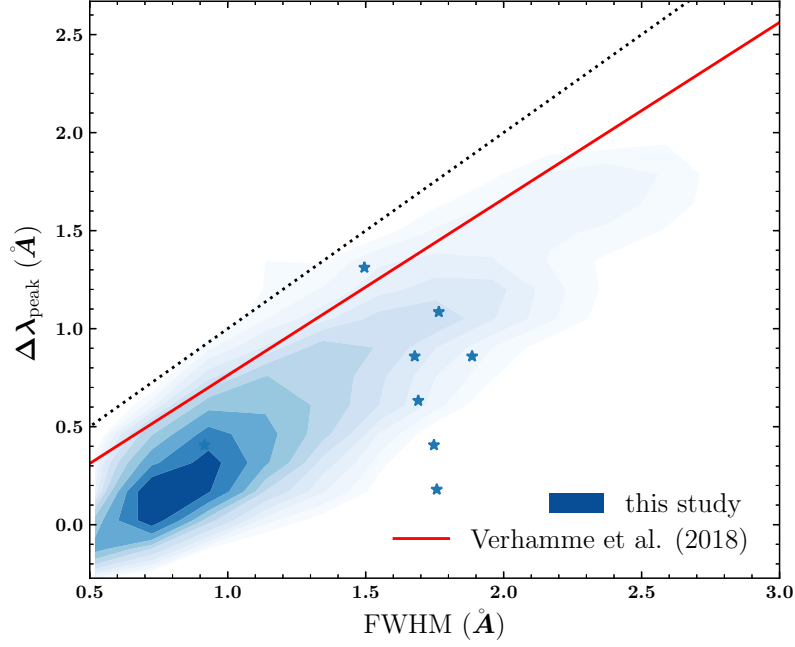


Figure 10. Distribution of peak shift and FWHM of simulated Ly α spectra of our 13,230 simulation runs (blue contours). Contour levels are in log scale. Blue stars are for the best-fit spectra of the MUSE galaxies examined in this study. Red solid line represents the empirical relation found by Verhamme et al. (2018) in observation, and black dotted line represents $y = x$ line.

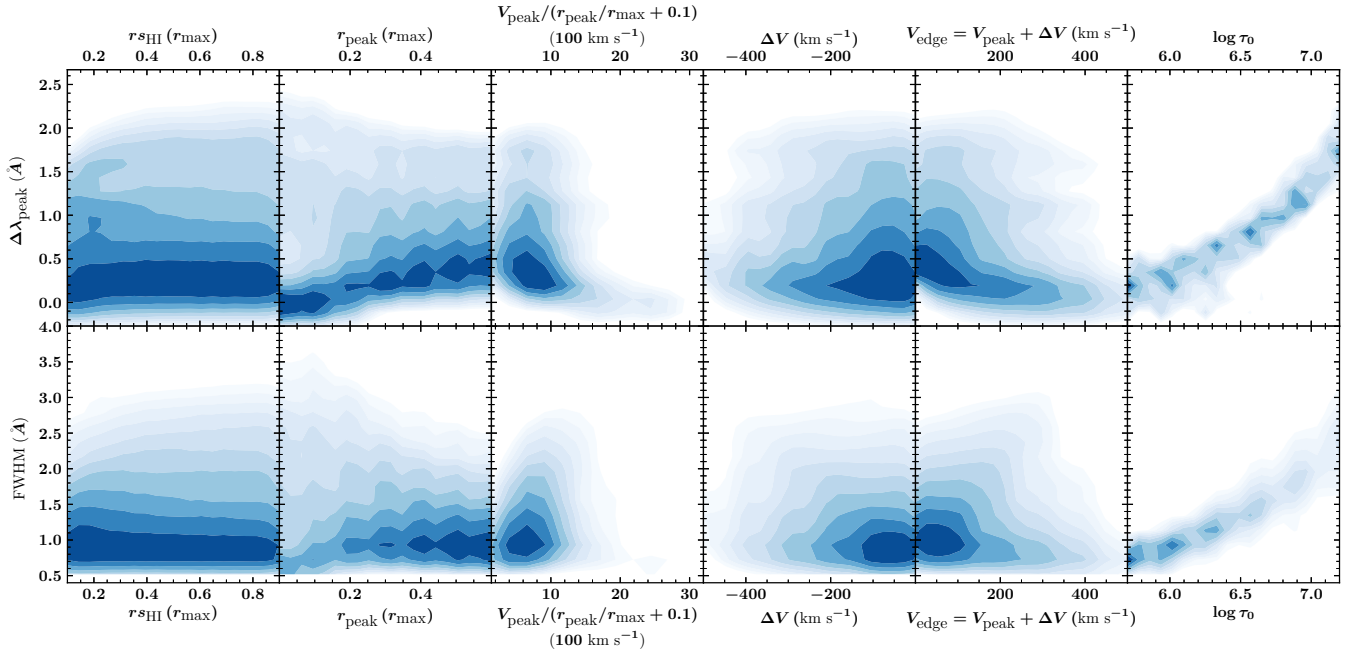


Figure 11. Correlation between peak shift ($\Delta\lambda_{\text{peak}}$) and other parameters (upper row), and FWHM and other parameters (lower row).

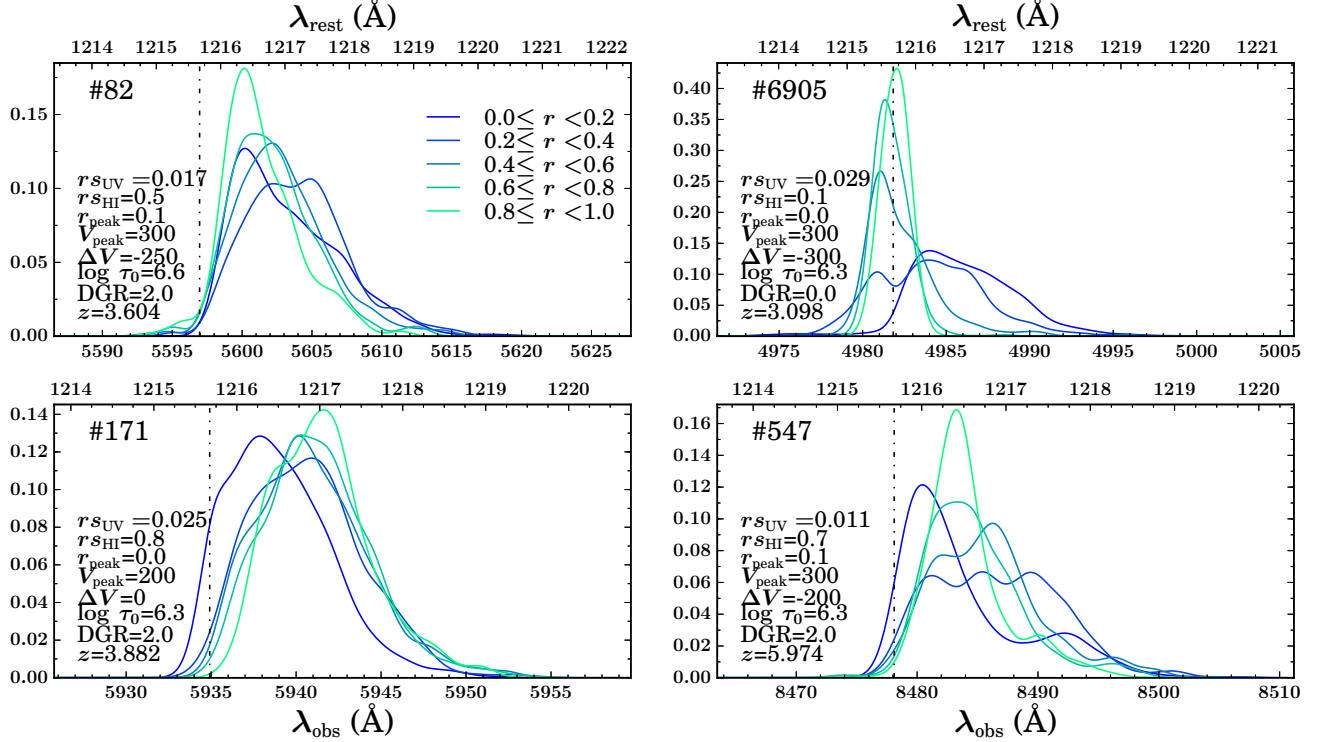


Figure 12. Simulated spectra at 5 annuli of different radii from the galaxy center for four target galaxies with their best-fit parameter set. Each MUSE id is written in top left of each panel and dot-dashed line represents the Ly α central wavelength.

optical-depth is larger than that of the Doppler frequency shift). This may also cause a negative correlation between FWHM and medium velocity, but this does not seem to be the case. It is because our velocity profile spans a range of velocity (unlike a constantly-expanding velocity profile) that becomes broader as peak velocity increases. Therefore, when peak velocity is larger, Ly α photons are Doppler-shifted to a larger range of wavelength in the rest frame of medium, which ends up with a larger FWHM. This again indicates that the peak shift–FWHM correlation could play a role in discriminating models, especially regarding velocity profile.

4.6. Spatially Resolved Ly α Spectra

One advantage of using the MUSE observational data is that we can obtain spatially resolved spectra. Unfortunately only (spatially) integrated spectra are publicly available for now, but it is still worth examining simulated spectra as a function of (projected) distance from the galaxy center. Figure 12 shows the simulated Ly α spectra measured at annuli of different radii with the best-fit parameter set for four target galaxies. Each spectrum is normalized by the total number of Ly α photons at each annulus. Because the true intensity level of spectra is imprinted in the surface brightness profile, here we examine only their shape. The results show that the shape of these spectra varies significantly with the radius, indicating that such spatially resolved spectra can be additionally used to infer spatial and kinematic distributions of medium in more detail.

In the case of MUSE #171, which is a relatively simple case with a constant expanding velocity, the different spectra at different locations are because of difference in the number of scatterings that photons have undergone until their escape. The peak of the spectrum tends to appear at a longer wavelength when the spectrum is measured at a larger distance from the galaxy center. Therefore, a larger shift of the spectral peak at a larger distance indicates that these photons escape after more scatterings. This makes sense because these photons come across longer distances from the central part, being scattered more to reach that the larger radii and then being able to escape there.⁶

The frequency shift (with respect to the initial frequency) of escaping photons could be larger not only when optical

⁶ Although we assume a spatially extended Ly α source distribution, emission is mostly from the central region (i.e., the scale radius for UV continuum emission of our target galaxies is smaller than 5% of the maximum extent of the system). Therefore, on-site emission at large radii accounts for only a small fraction, and the majority are those scattered from the central region, which had been scattered many times to reach large radii.

depth is larger but also when the medium moves faster, if the medium velocity is not too high (see Appendix D). For other target galaxies, the peak shift of spectrum tends to become larger and then smaller as the radius increases. Such a behavior of the peak shift could be attributed to the velocity profile that increases and then decreases as the distance from the galaxy center increases. However, it should be noted that if the medium velocity is too large, photons can escape the system without many scatterings, so the behavior of the peak shift as a function of radius could not be easily understood. It should be also noted that the annuli where we obtain the spectra are in the projected space. Therefore, the spectrum at a small radius consists of photons that are emerging at a large range of three-dimensional distance, which possibly makes multiple peaks in the spectrum as seen in most of our target galaxies. Such a feature will be useful for extracting kinematic information of the medium, especially its spatial variation, from observational data.

Although the parameters of the medium velocity field help us to understand the overall trend of spectra from different annuli, we need to consider other factors as well, especially $r_{s_{H\text{ I}}}$ and τ_0 to understand the phenomena in more detail. For example, the combination of small $r_{s_{H\text{ I}}}$ and small τ_0 for the case of MUSE #6905 leads to so few scatterings at large radii that the spectrum at the outermost annuli shows almost no shift even though the medium is completely static at the edge. The peak of spectra from the outer part of the galaxy shows a slight shift to the blue side because the expanding velocity profile of medium always decreases (i.e., $r_{\text{peak}} = 0$).

In summary, Ly α spectra from different positions in and around a galaxy are quite distinguishable, of which degree is determined by the interplay of multiple parameters regarding the spatial and kinematic distributions of medium. Therefore, spatially resolved Ly α spectra could give much tighter constraints on the parameters than an integrated spectrum. We will continue our work in this direction.

4.7. Impacts of Ly α Input Spectrum on Emerging Spectrum and Surface Brightness Profile

To perform Ly α Monte Carlo radiative transfer calculations, we set the input Ly α spectrum as a Voigt profile with a temperature of 10^4K , the typical temperature of H II regions. All the results we show in this paper are based on this input spectrum. In other words, we performed the Ly α radiative transfer calculation only in the diffuse interstellar medium and the circumgalactic medium, ignoring the radiative transfer in H II regions. However, in reality, for instance, some bulk outflowing motion induced by stellar winds in H II regions could give rise to asymmetric double-peak spectra (Kimm et al. 2019).

There are many possible options for the input spectrum, which include a Gaussian profile, a symmetric double-peak profile, and one including continuum with different line strengths (i.e., different EWs). However, we consider only an asymmetric double-peak profile of which red peak is stronger than the blue one, as suggested by Kimm et al. (2019). We approximate the asymmetric double-peak profiles in Kimm et al. (2019) using a sum of two Voigt profiles; each of them is shifted by Δx toward red and blue, respectively, and the red peak is two times stronger than the blue one. Although our approximation is not precisely mimicking those in Kimm et al. (2019), we do expect to draw a qualitatively consistent conclusion with the case by adopting the exact form of their spectra.

We construct Ly α spectrum and surface brightness profile using the asymmetric double-peak profile as an input spectrum, which is easily done by adjusting the weight of each photon, following the procedure described in Section 2.1. We consider different cases with four peak separations ($2\Delta x$ where $\Delta x = 0, 5, 10, 15$, and $\Delta x = 0$ corresponds to a pure Voigt profile), and implement each case by putting $V(x + \Delta x) + 0.5V(x - \Delta x)$ for \mathcal{S}_f in Eqn. (1) where $V(x)$ represents a Voigt profile. Figure 13 shows the Ly α spectra and surface brightness profiles of the four different peak separations for two galaxies with their best-fit parameter set. As the two peaks of the input spectrum are farther away from the central wavelength (i.e., as Δx increases), the emerging spectrum becomes sharper and the surface brightness profile becomes steeper. The photons on the red side in the input spectrum become even redder (i.e., farther away from the central wavelength) in the medium frame because of the expanding velocity; they are rarely scattered and emerging at their initial frequencies. On the other hand, the photons on the blue side become less blue (i.e., closer to the central wavelength); they escape after a lot of scatterings, forming a broad component. In the result, the emerging spectrum tends to have a sharper peak with a larger shift as the peak separation increases. In the case of surface brightness profile, as the two peaks of the input spectrum are farther away from the central wavelength, the majority (red photons) are less scattered, which results in a steeper profile. It should be noted that the details will be determined by effective optical-depth. When the effective optical-depth is large, the change in the emerging spectrum due to the variation of the input spectrum will be small because a large number of scatterings tend to erase the information of the initial frequency distribution. (e.g., the case of MUSE #1343).

The best fit for each target galaxy will be quite different from that in Table 3 if we adopt such an asymmetric (red-dominant) double-peak spectrum as an input spectrum. We expect that a parameter set that gives a larger effective

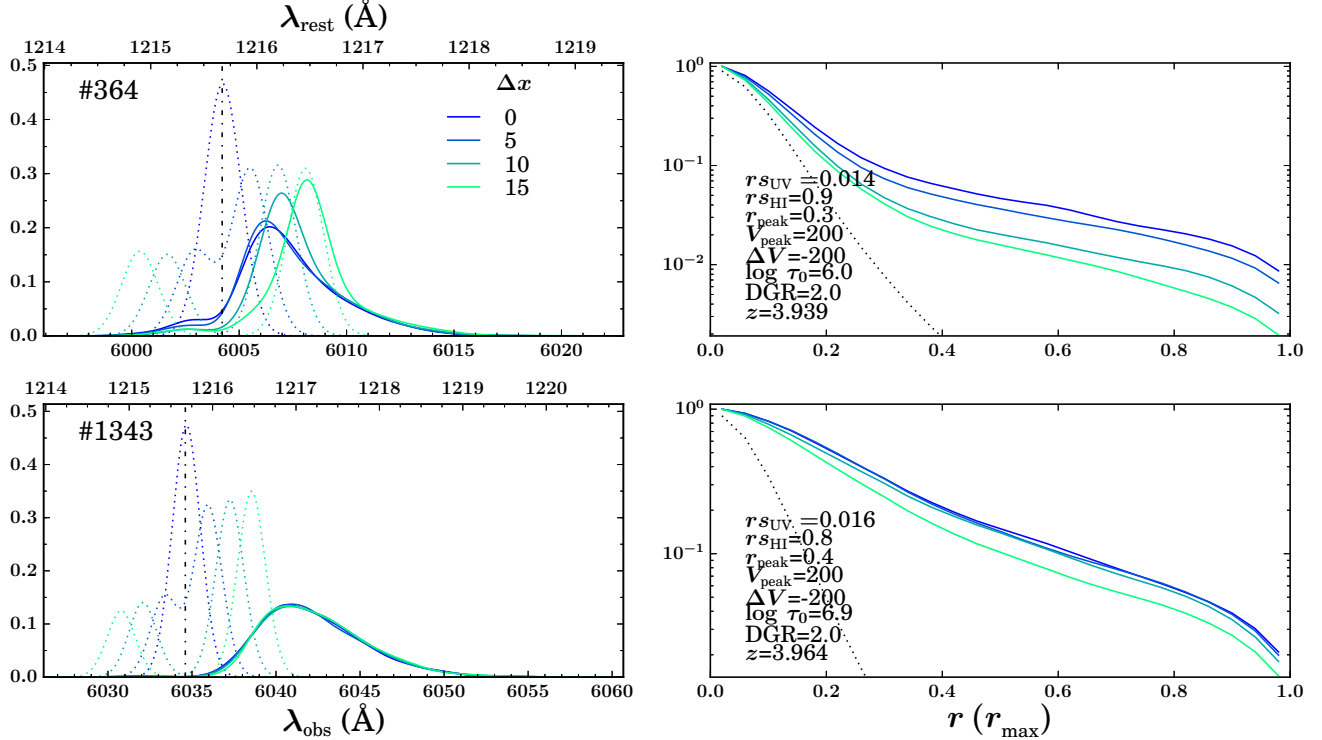


Figure 13. Similar to Figure 8, but with varying Δx (the offset of each peak from the central wavelength for the input Ly α spectrum). In the spectrum panels, dotted lines are for different input spectra of different Δx values.

optical-depth (i.e., larger optical depth and smaller expanding velocities) will be preferred to remove a sharp peak with a large shift. It is important to have a better idea on the Ly α input spectrum for more accurate modeling in small spatial scales. One more thing we should notice is that previous studies varied the width of the input Ly α spectrum, incorporating turbulent motion. However, we could successfully model the data without considering this effect.

5. SUMMARY

We perform Ly α radiative transfer calculations with an outflowing halo model that is improved from a simple, constantly-expanding shell model⁷. We reproduce successfully Ly α properties (i.e., spectrum and surface brightness profile) of eight star-forming galaxies at $z=3-6$ observed with MUSE, of which results are consistent with the results from other studies. We summarize our results as follows.

- The constraints on the model parameters are largely improved by using spectrum and surface brightness profile simultaneously. This is because spectrum and surface brightness profile change diversely and independently with each model parameter, which helps breaking degeneracies between the model parameters.
- We examine spatially resolved Ly α spectra emerging at different distances from the galactic center. The spectral shape (e.g., the position and the number of spectral peaks and width) changes with distance. The changes can be understood with a given model parameter set, which provides a basis of using spatially resolved spectra to better infer density and velocity fields of circumgalactic medium from observations.
- The individual model parameters change Ly α spectrum and surface brightness profile in a various way. The changes in Ly α spectrum and surface brightness profile by each model parameter could be significant or not depending on other parameter values. However, the impacts of optical depth and redshift on Ly α spectrum and surface brightness profile are always apparent.
- There is degeneracy between model parameters, which can be understood from the changes of Ly α spectrum and surface brightness profile with each model parameter. The most prominent ones are optical depth–the radius of

⁷ The numerical data of the present models will be made available at https://data.kasi.re.kr/vo/LaRT_models/.

peak expanding velocity and optical depth–redshift in determining the spectrum. The parameter degeneracy in determining the surface brightness profile appears weak in general, which is mainly because of the poor parameter constraints of surface brightness profile.

- Dust does have impacts on the shape of Ly α spectrum due to differential intensity reductions depending on wavelengths. This is because Ly α spectrum consists of Ly α photons escaping after different numbers of scatterings that systematically change with emerging wavelengths. However, such impacts of dust become significant when the effective optical-depth is large.
- We examine correlations between model parameters and the observed properties of high-redshift Ly α galaxies. The spatial extent of Ly α halos shows strong correlations with the spatial extents of UV emission and neutral hydrogen medium, and bulk velocities of medium. The positive correlation between peak shift and FWHM of Ly α spectrum is well reproduced by our simulations. The peak shift–FWHM correlation could provide an additional constraint on the velocity profile of medium.
- Ly α input spectrum is an important factor that determines the shapes of emerging spectrum and surface brightness profile (in particular for H II regions with relatively low optical depth). We test the case of a red-dominant double-peak input spectrum for various peak separations, which results in systematic changes in the emerging spectrum and the surface brightness profile. This suggests that model parameter constraints could vary largely depending on the choice of Ly α input spectrum.

This study is the first attempt to model the observed Ly α spectrum and surface brightness profile simultaneously. We will extend our analyses to a larger sample to characterize physical parameters of high-redshift Ly α -emitting galaxies with better statistics.

We thank to the referee for his/her careful reading and the constructive comments. This work was supported by the National Research Foundation of Korea (NRF) grant funded by the Korean government (MSIP) (No. 2017R1A2B4008291). This work was also supported by the National Institute of supercomputing and Network/Korea Institute of Science and Technology Information with supercomputing resources including technical supporting (KSC-2018-S1-0005). HSong would like to thank Minsu Shin, Yujin Yang, Max Gronke, and Clotilde Laigle for useful discussions and advices.

REFERENCES

- Ahn, S.-H. 2004, *ApJL*, 601, L25
- Ahn, S.-H., Lee, H.-W., & Lee, H. M. 2000, *Journal of Korean Astronomical Society*, 33, 29
- . 2002, *ApJ*, 567, 922
- Bacon, R., Brinchmann, J., Richard, J., et al. 2015, *A&A*, 575, A75
- Bacon, R., Conseil, S., Mary, D., et al. 2017, *A&A*, 608, A1
- Behrens, C., Dijkstra, M., & Niemeyer, J. C. 2014, *A&A*, 563, A77
- Cantalupo, S., Porciani, C., Lilly, S. J., & Miniati, F. 2005, *ApJ*, 628, 61
- Carswell, R. F., & Webb, J. K. 2014, VPFIT: Voigt profile fitting program, ascl:1408.015
- Charlot, S., & Fall, S. M. 1993, *ApJ*, 415, 580
- Claeysens, A., Richard, J., Blaizot, J., et al. 2019, *MNRAS*, 489, 5022
- Cowie, L. L., & Hu, E. M. 1998, *AJ*, 115, 1319
- Dijkstra, M. 2017, arXiv e-prints, arXiv:1704.03416
- Dijkstra, M., Haiman, Z., & Spaans, M. 2006a, *ApJ*, 649, 14
- . 2006b, *ApJ*, 649, 14
- Dijkstra, M., & Kramer, R. 2012, *MNRAS*, 424, 1672
- Draine, B. T. 2003, *ARA&A*, 41, 241
- Drake, A. B., Guiderdoni, B., Blaizot, J., et al. 2017, *MNRAS*, 471, 267
- Duval, F., Schaerer, D., Östlin, G., & Laursen, P. 2014, *A&A*, 562, A52
- Erb, D. K., Steidel, C. C., & Chen, Y. 2018, *ApJL*, 862, L10
- Fynbo, J. U., Møller, P., & Warren, S. J. 1999, *MNRAS*, 305, 849
- Garel, T., Blaizot, J., Guiderdoni, B., et al. 2012, *Monthly Notices of the Royal Astronomical Society*, 422, 310
- Gronke, M. 2017, *A&A*, 608, A139
- Gronke, M., Bull, P., & Dijkstra, M. 2015, *ApJ*, 812, 123
- Hansen, M., & Oh, S. P. 2006, *MNRAS*, 367, 979
- Harrington, J. P. 1973, *MNRAS*, 162, 43
- Hartmann, L. W., Huchra, J. P., Geller, M. J., O’Brien, P., & Wilson, R. 1988, *ApJ*, 326, 101
- Hayes, M., Östlin, G., Schaerer, D., et al. 2013, *ApJL*, 765, L27
- Henye, L. G., & Greenstein, J. L. 1941, *ApJ*, 93, 70
- Karman, W., Caputi, K. I., Caminha, G. B., et al. 2017, *A&A*, 599, A28
- Kimm, T., Blaizot, J., Garel, T., et al. 2019, *MNRAS*, 486, 2215
- Kunth, D., Mas-Hesse, J. M., Terlevich, E., et al. 1998, *A&A*, 334, 11
- Laursen, P., Duval, F., & Östlin, G. 2013, *ApJ*, 766, 124
- Leclercq, F., Bacon, R., Wisotzki, L., et al. 2017, *A&A*, 608, A8
- Leclercq, F., Bacon, R., Verhamme, A., et al. 2020, *A&A*, 635, A82
- Loeb, A., & Rybicki, G. B. 1999, *ApJ*, 524, 527
- Mas-Hesse, J. M., Kunth, D., Tenorio-Tagle, G., et al. 2003, *ApJ*, 598, 858
- Matsuda, Y., Yamada, T., Hayashino, T., et al. 2012, *MNRAS*, 425, 878
- Meier, D. L., & Terlevich, R. 1981, *ApJL*, 246, L109

- Michel-Dansac, L., Blaizot, J., Garel, T., et al. 2020, *A&A*, 635, A154
- Møller, P., Fynbo, J. P. U., & Fall, S. M. 2004, *A&A*, 422, L33
- Momose, R., Ouchi, M., Nakajima, K., et al. 2014, *MNRAS*, 442, 110
- . 2016, *MNRAS*, 457, 2318
- Neufeld, D. A. 1990, *ApJ*, 350, 216
- Noll, S., Mehlert, D., Appenzeller, I., et al. 2004, *A&A*, 418, 885
- Orlitová, I., Verhamme, A., Henry, A., et al. 2018, *A&A*, 616, A60
- Östlin, G., Hayes, M., Duval, F., et al. 2014, *ApJ*, 797, 11
- Ouchi, M., Harikane, Y., Shibuya, T., et al. 2018, *PASJ*, 70, S13
- Partridge, R. B., & Peebles, P. J. E. 1967, *ApJ*, 147, 868
- Prochaska, J. X., Kasen, D., & Rubin, K. 2011, *ApJ*, 734, 24
- Rhoads, J. E., Malhotra, S., Dey, A., et al. 2000, *ApJL*, 545, L85
- Richling, S. 2003, *MNRAS*, 344, 553
- Schaerer, D., Hayes, M., Verhamme, A., & Teyssier, R. 2011, *A&A*, 531, A12
- Schaerer, D., & Verhamme, A. 2008, *A&A*, 480, 369
- Seon, K.-I., & Draine, B. T. 2016, *ApJ*, 833, 201
- Seon, K.-I., & Kim, C.-G. 2020, arXiv e-prints, arXiv:2005.00238
- Shapley, A. E., Steidel, C. C., Adelberger, K. L., & Pettini, M. 2003, in *Revista Mexicana de Astronomia y Astrofisica Conference Series*, ed. V. Avila-Reese, C. Firmani, C. S. Frenk, & C. Allen, Vol. 17, 254–255
- Spaans, M. 1996, *A&A*, 307, 271
- Steidel, C. C., Bogosavljević, M., Shapley, A. E., et al. 2011, *ApJ*, 736, 160
- Steidel, C. C., Erb, D. K., Shapley, A. E., et al. 2010, *The Astrophysical Journal*, 717, 289
- Strauss, M. A., Weinberg, D. H., Lupton, R. H., et al. 2002, *AJ*, 124, 1810
- Sunyaev, R. A., Tinsley, B. M., & Meier, D. L. 1978, *Comments on Astrophysics*, 7, 183
- Tapken, C., Appenzeller, I., Mehlert, D., Noll, S., & Richling, S. 2004, *A&A*, 416, L1
- Tasitsiomi, A. 2006, *ApJ*, 645, 792
- Tenorio-Tagle, G., Silich, S. A., Kunth, D., Terlevich, E., & Terlevich, R. 1999, *MNRAS*, 309, 332
- Valls-Gabaud, D. 1993, *ApJ*, 419, 7
- Vanzella, E., Grazian, A., Hayes, M., et al. 2010, *A&A*, 513, A20
- Venemans, B. P., Röttgering, H. J. A., Miley, G. K., et al. 2005, *A&A*, 431, 793
- Verhamme, A., Orlitová, I., Schaerer, D., & Hayes, M. 2015, *A&A*, 578, A7
- Verhamme, A., Schaerer, D., Atek, H., & Tapken, C. 2008, *A&A*, 491, 89
- Verhamme, A., Schaerer, D., & Maselli, A. 2006, *A&A*, 460, 397
- Verhamme, A., Garel, T., Ventou, E., et al. 2018, *MNRAS*, 478, L60
- Weingartner, J. C., & Draine, B. T. 2001, *ApJ*, 548, 296
- Wilman, R. J., Gerssen, J., Bower, R. G., et al. 2005, *Nature*, 436, 227
- Wisotzki, L., Bacon, R., Blaizot, J., et al. 2016, *A&A*, 587, A98
- Witt, A. N. 1977, *ApJS*, 35, 1
- Yang, H., Malhotra, S., Gronke, M., et al. 2016, *ApJ*, 820, 130
- Yang, H., Malhotra, S., Rhoads, J. E., et al. 2017, *ApJ*, 838, 4
- Zheng, Z., & Miralda-Escudé, J. 2002, *ApJ*, 578, 33
- Zheng, Z., & Wallace, J. 2014, *ApJ*, 794, 116

APPENDIX

A. VALIDATION OF POST-PROCESSING DUST EFFECT

We assume that dust scattering is perfectly forward-directed for the post-processing of the dust effect. We examine whether this assumption is valid or not by comparing the escape fractions of Ly α photons when the effect of dust is fully taken into account in simulation from the beginning ($f_{\text{esc}}^{\text{full}}$) and when it is implemented through post-processing ($f_{\text{esc}}^{\text{PP}}$). The Ly α radiative transfer simulation is performed in an infinite, static slab of medium at a temperature 10^4K for the ranges of τ_0 and DGR of interest of this study. We consider a point, monochromatic source of Ly α . Figure 14 shows the ratio of $f_{\text{esc}}^{\text{PP}}/f_{\text{esc}}^{\text{full}}$ as functions of τ_0 and DGR. The post-processing approach tends to slightly underestimate the escape fraction, and the degree of underestimate increases with τ_0 and DGR. However, the amount of underestimation is less than $\sim 9\%$ even for the largest τ_0 and DGR (i.e., $\log \tau_0 = 7.2$ and $\text{DGR} = 2\text{DGR}_{\text{MW}}$), and these two treatments of dust show a good agreement in general. Therefore, the post-processing approach can be claimed as a good approximation to the full simulation approach. This is expected because the angular redistribution function for dust scattering in simulation is set to be the Henyey-Greenstein phase function, which is strongly forward-throwing. In summary, the assumption of perfect forward scattering by dust is valid at least for the ranges of τ_0 and DGR considered here, and so the application of post-processing the effect of dust is.

B. POSTERIOR DISTRIBUTIONS OF MODEL PARAMETERS (CONTINUED)

We present only total posterior distributions (\mathcal{L}_{tot}) for the rest seven target galaxies (Figures 15, 17, 19 23, 25, 27, and 29) for the sake of brevity. However, we present posterior distributions for spectrum (\mathcal{L}_{sp}) and surface brightness profile (\mathcal{L}_{SBP}) for MUSE #53 because it is a special case of its best-fit parameter set being determined solely by spectrum. Nevertheless, parameter constraints become tighter by including surface brightness profile, which is revealed by comparing Figures 23 and 21. The best-fit model spectrum and surface brightness profile determined with (\mathcal{L}_{tot}) for the seven galaxies are also shown in Figures 16, 18, 20, 24, 26, 28, and 30.

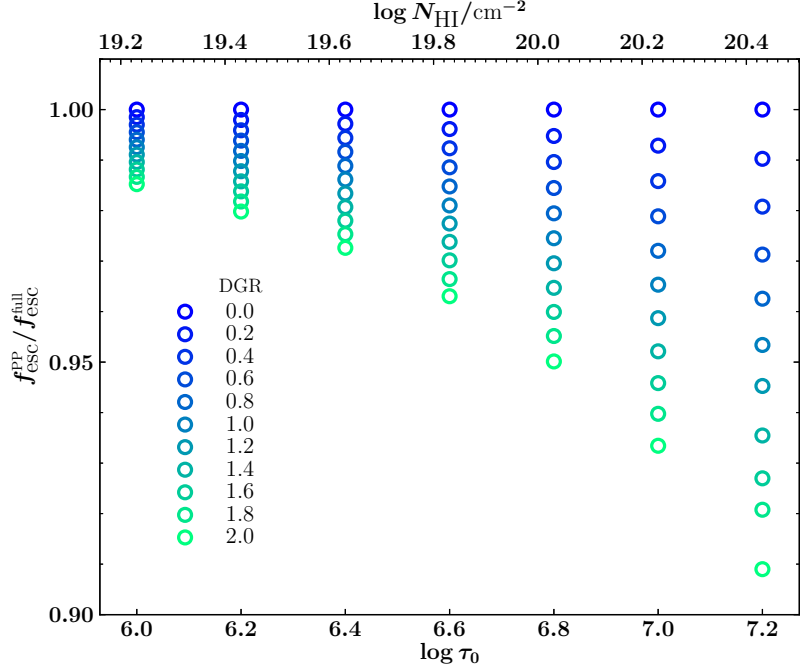


Figure A14.: The ratio of two estimates on the escape fraction of Ly α photons that are emitted from a point, monochromatic source and traveling through an infinity slab of temperature 10^4K as functions of τ_0 (x-axis) and DGR (denoted by colors): $f_{\text{esc}}^{\text{full}}$ is obtained when the effect of dust is fully simulated and $f_{\text{esc}}^{\text{PP}}$ is when the effect of dust is post-processed.

C. LY α SPECTRUM AND SURFACE BRIGHTNESS PROFILE VARIATION IN MODEL PARAMETER SPACE (CONTINUED)

In this section, we present the impact of the rest of model parameters on the shapes of spectrum and surface brightness profile that are not fully presented in Section 4.3.

Figure 31 shows the changes of spectrum and surface brightness profile with r_{peak} . The spectrum tends to be broader with higher intensities at the central wavelength and at the red wing as r_{peak} decreases (see the case of MUSE #6905). The higher intensity at the central wavelength is because the inner medium becomes more transparent with a larger expanding velocity at a given radius when r_{peak} is smaller, thus letting more photons at the central wavelength to escape from the system without scatterings. The higher intensities at the red wing for smaller r_{peak} is because photons are more likely to be scattered by larger velocities, and thus are scattered into wavelengths farther away from the central wavelength. A surface brightness profile tends to be flatter at small radii when r_{peak} is larger (because of more scatterings there), but its trend with r_{peak} at large radii seems to depend on other parameters. When the outer part of the galaxy is optically thick (with large $r_{\text{SH I}}$, small ΔV , and large τ_0), the change of spectrum with r_{peak} becomes negligible and the flattening of surface brightness profile by increasing r_{peak} extends to a large radius (e.g., MUSE #1343).

We can speculate the changes of spectrum and surface brightness profile with V_{peak} on the analogy of those with r_{peak} . Increasing V_{peak} has an effect similar to decreasing r_{peak} , making the medium more transparent at a given radius. Therefore, as V_{peak} increases, a spectrum will have a sharper peak that is closer to the central wavelength and a broader red tail. A surface brightness profile becomes steeper with V_{peak} . These trends are well shown in Figure 32 as expected. Compared to the case of r_{peak} , the impact of V_{peak} on both spectrum and surface brightness profile is more significant. It is because the maximum levels of medium transparency and the frequency change that can be reached by varying r_{peak} are limited by a given V_{peak} value. Moreover, it is limited to $r < r_{\text{peak}}$ that the medium becomes more transparent as r_{peak} decreases. The medium at $r > r_{\text{peak}}$ becomes less transparent as r_{peak} decreases. However, increasing V_{peak} makes the whole medium more transparent.

The impact of ΔV on spectrum and surface brightness profile is presented in Figure 33. The change of surface brightness profile with ΔV is obvious; as ΔV decreases (i.e., as the velocity at the edge decreases closer to zero), the

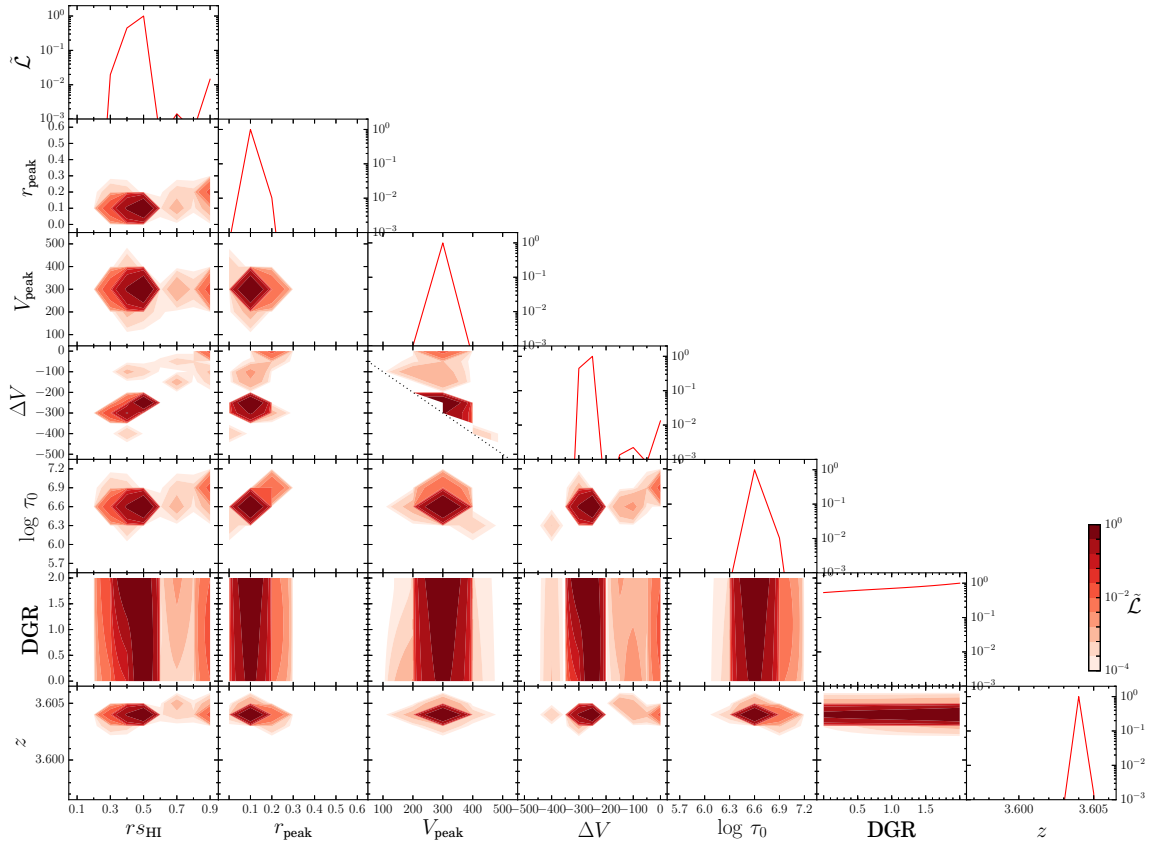


Figure B15.: Similar to Figure 5, but for MUSE #82.

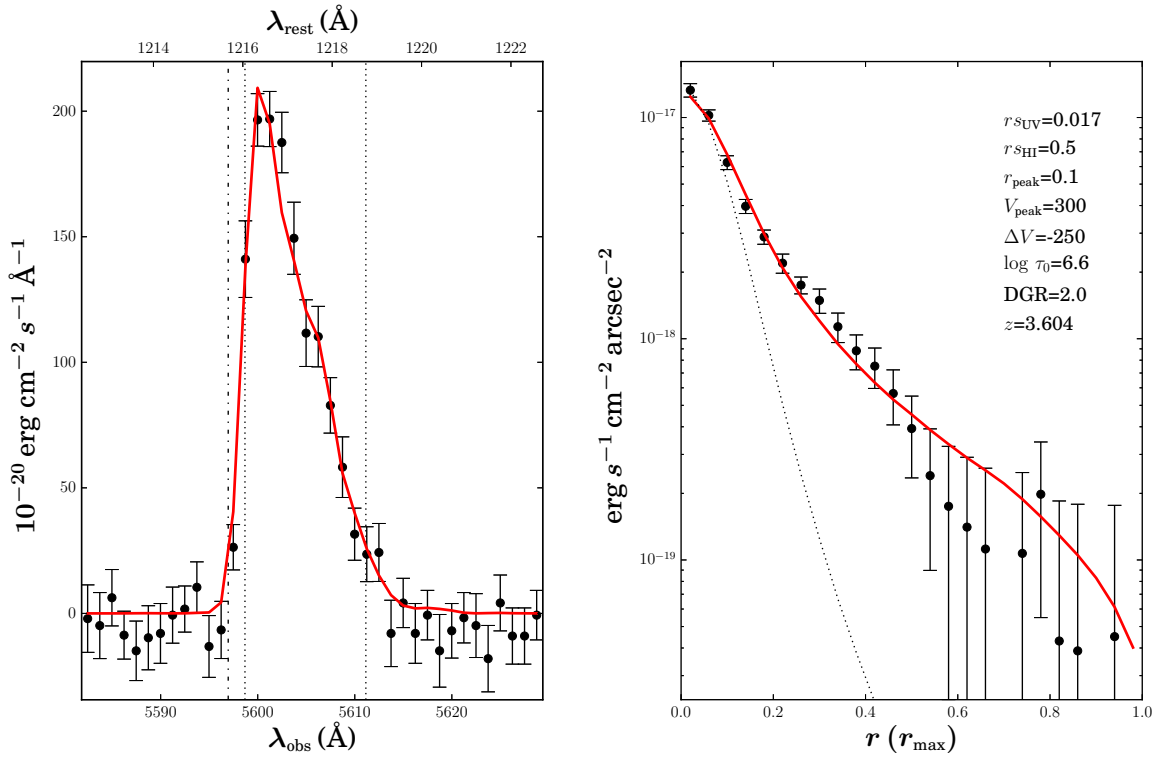


Figure B16.: Similar to Figure 6, but for MUSE #82.

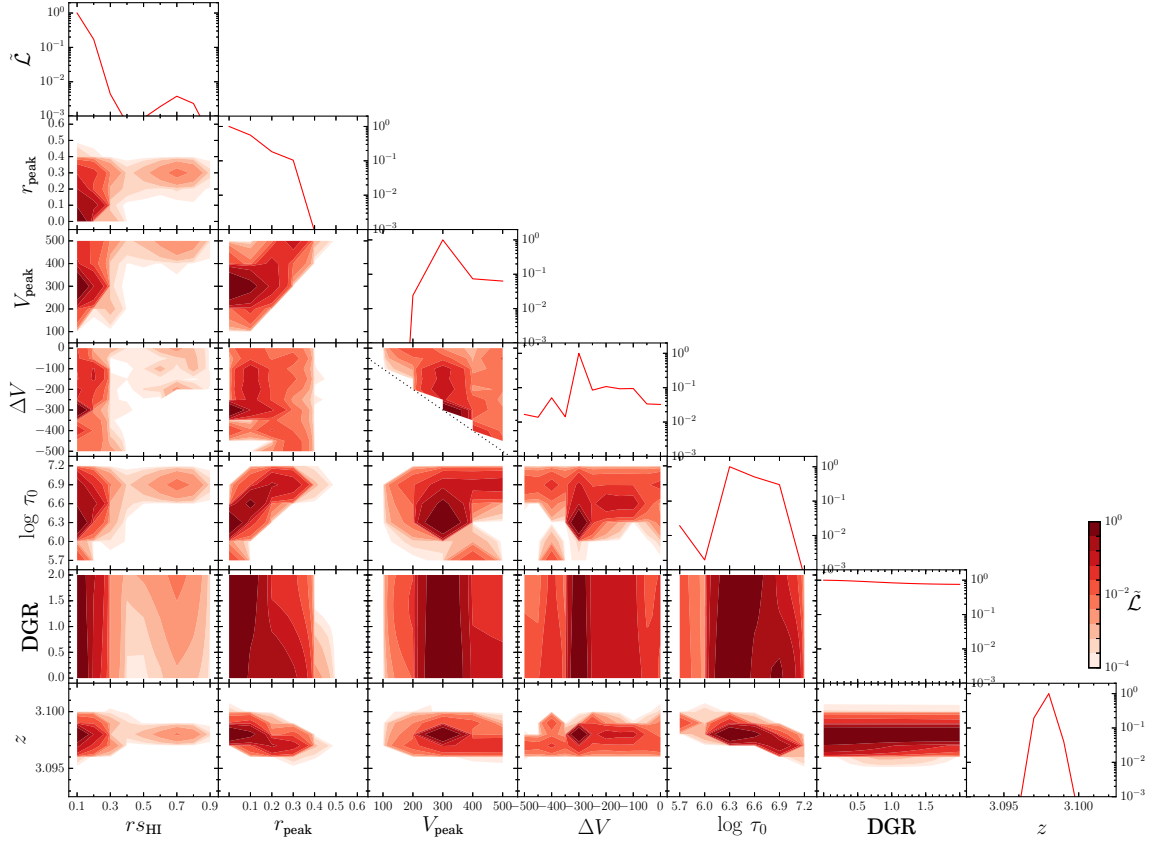


Figure B17:. Similar to Figure 5, but for MUSE #6905.

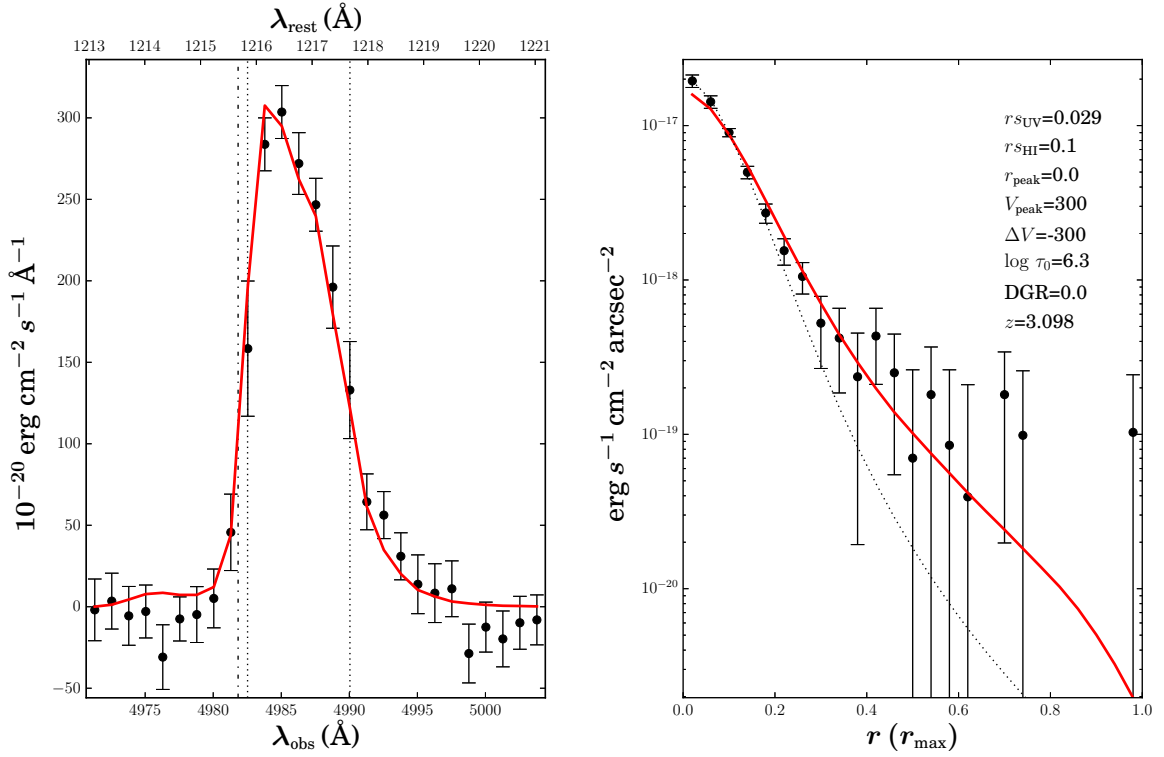


Figure B18:. Similar to Figure 6, but for MUSE #6905.

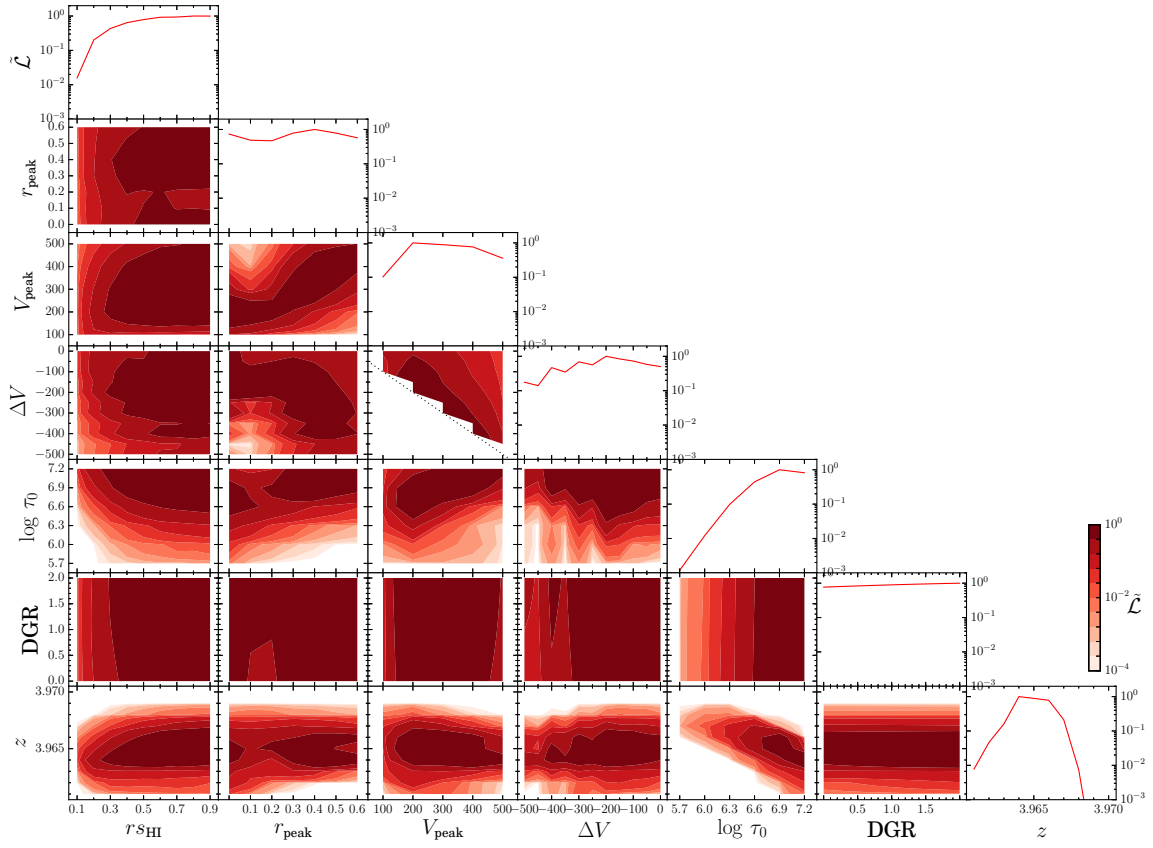


Figure B19:. Similar to Figure 5, but for MUSE #1343.

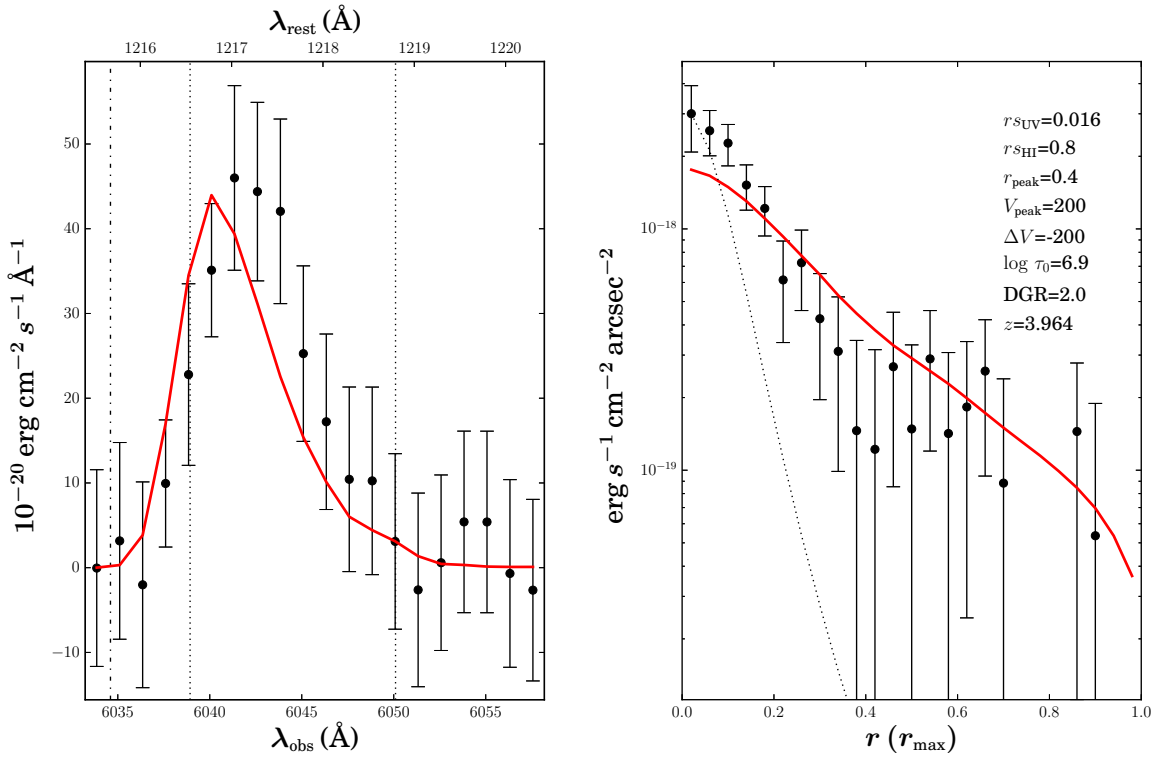


Figure B20:. Similar to Figure 6, but for MUSE #1343.

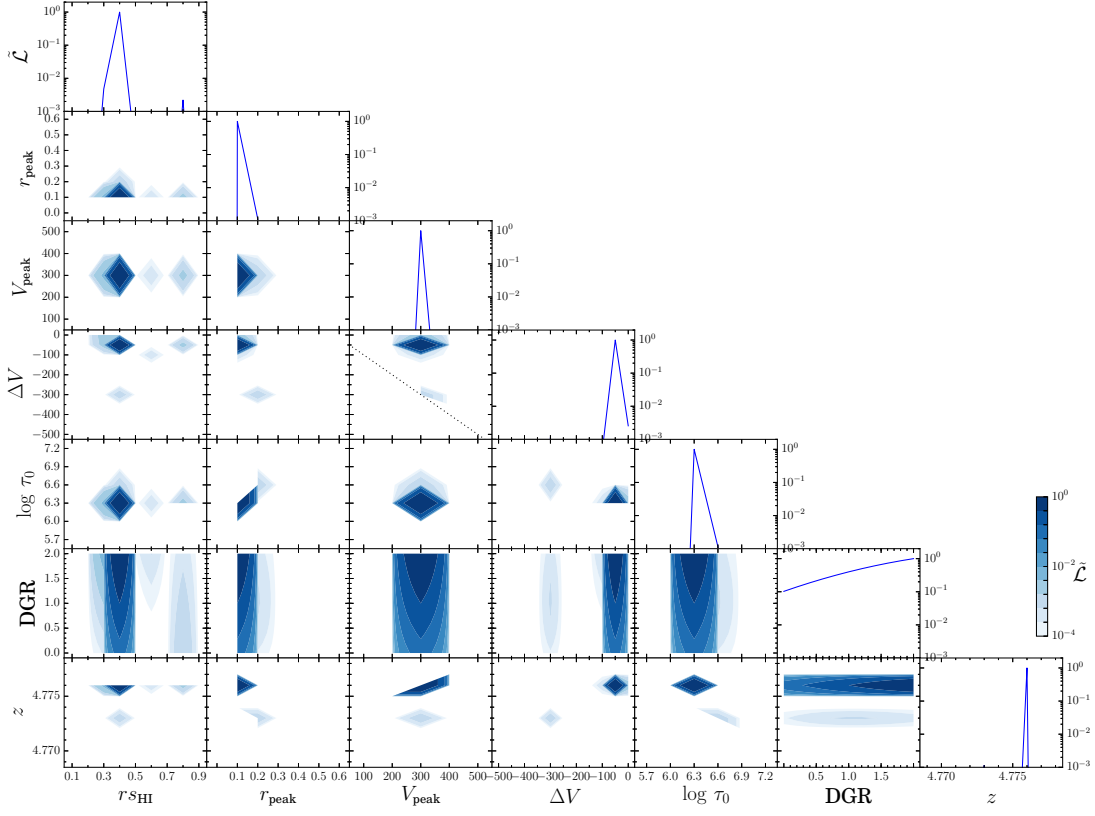


Figure B21.: Similar to Figure 1, but for MUSE #53.

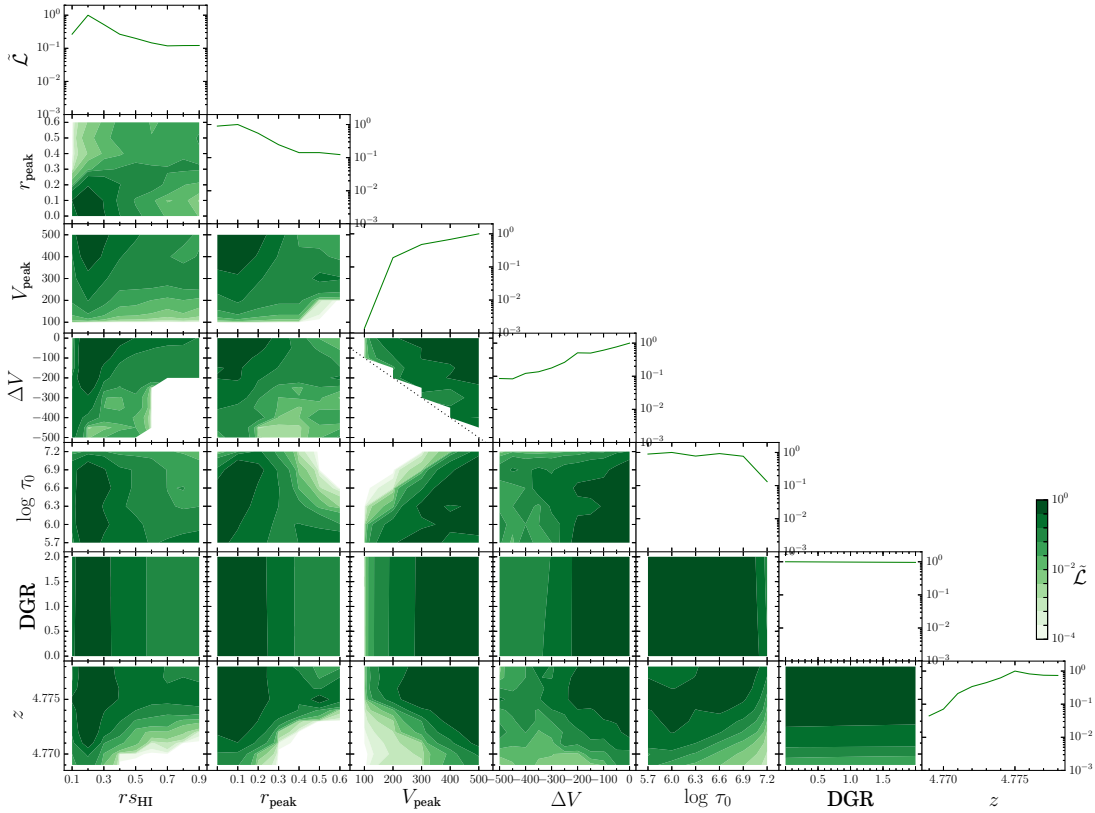


Figure B22.: Similar to Figure 2, but for MUSE #53.

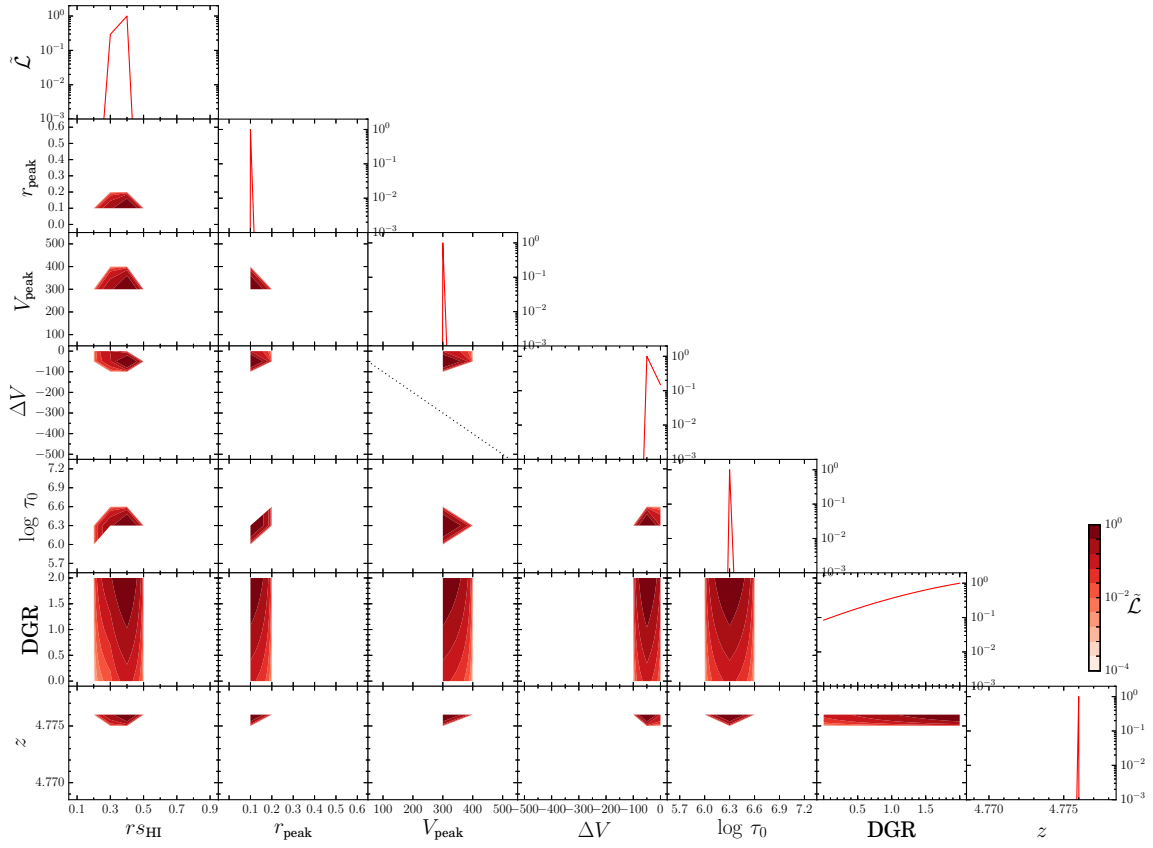


Figure B23:. Similar to Figure 5, but for MUSE #53.

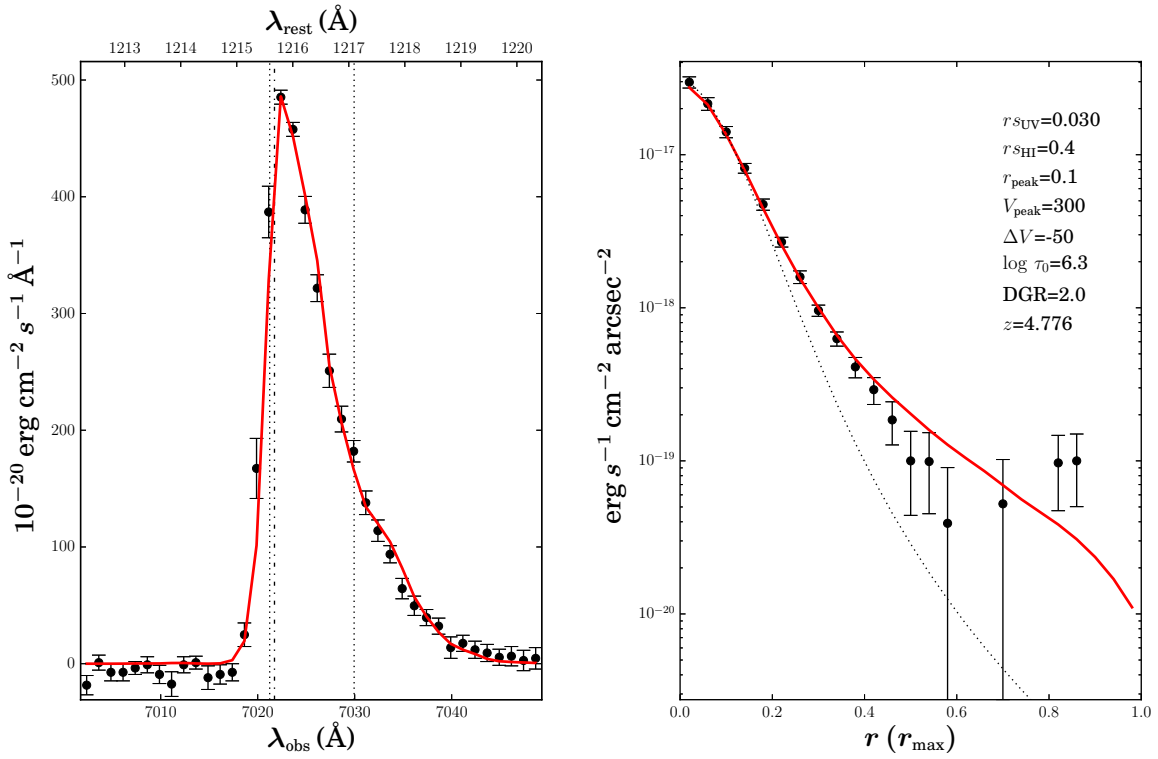


Figure B24:. Similar to Figure 6, but for MUSE #53.

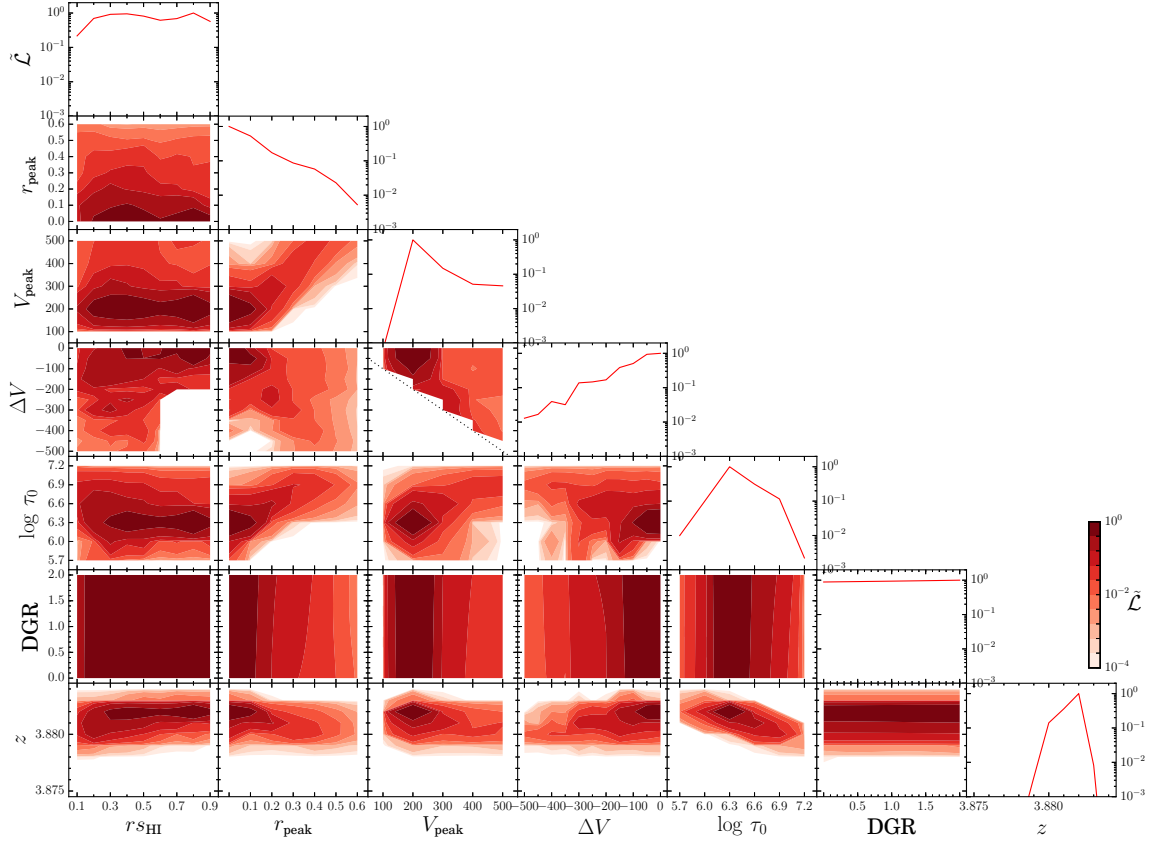


Figure B25:. Similar to Figure 5, but for MUSE #171.

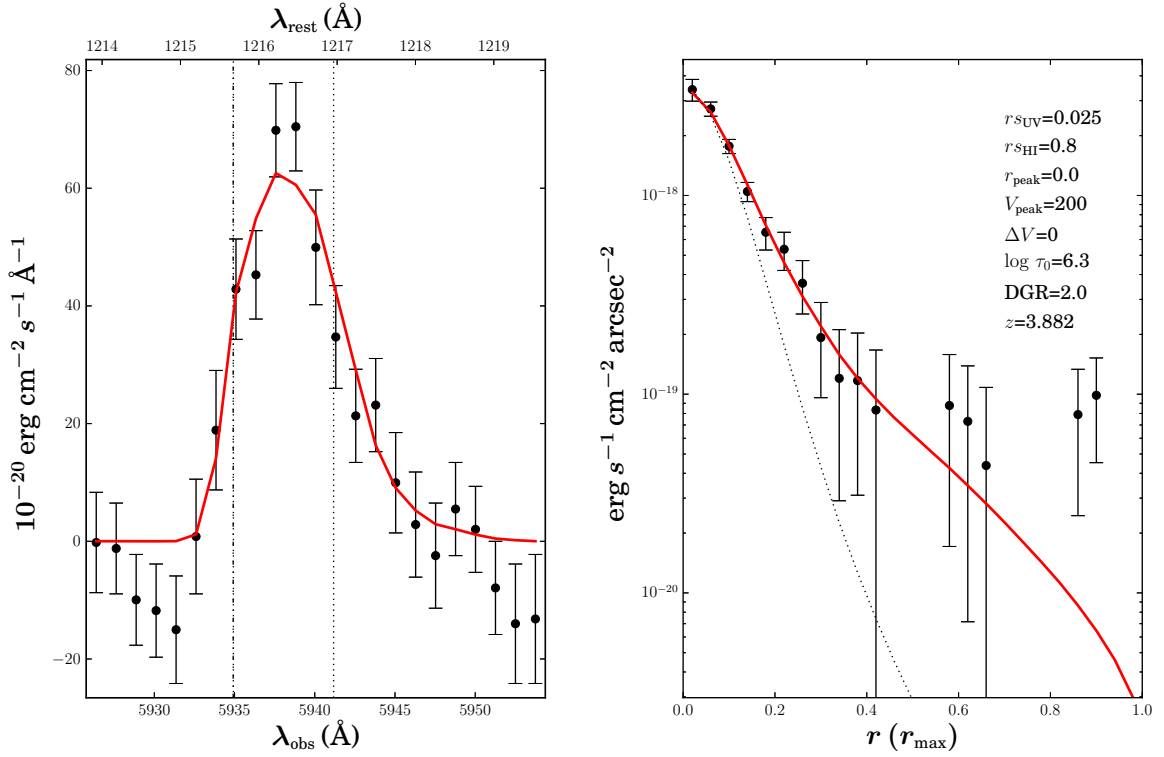


Figure B26:. Similar to Figure 6, but for MUSE #171.

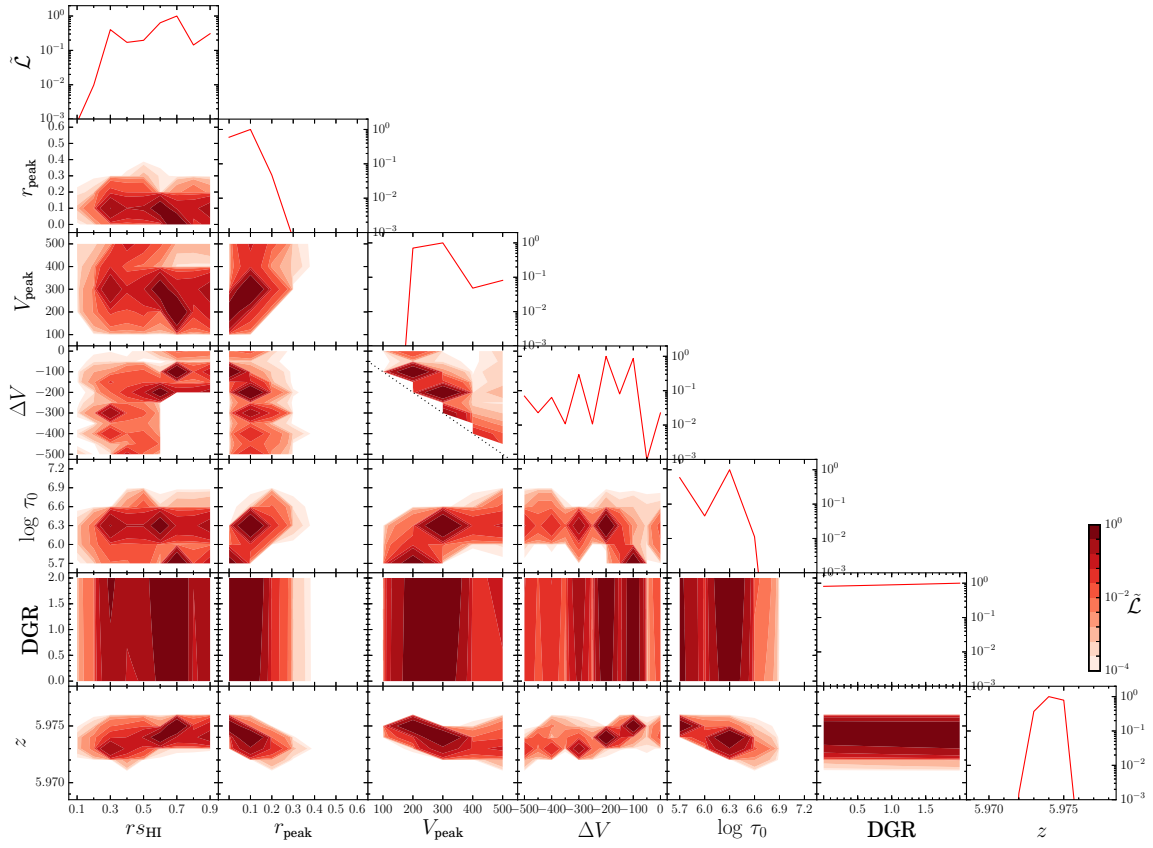


Figure B27:. Similar to Figure 5, but for MUSE #547.

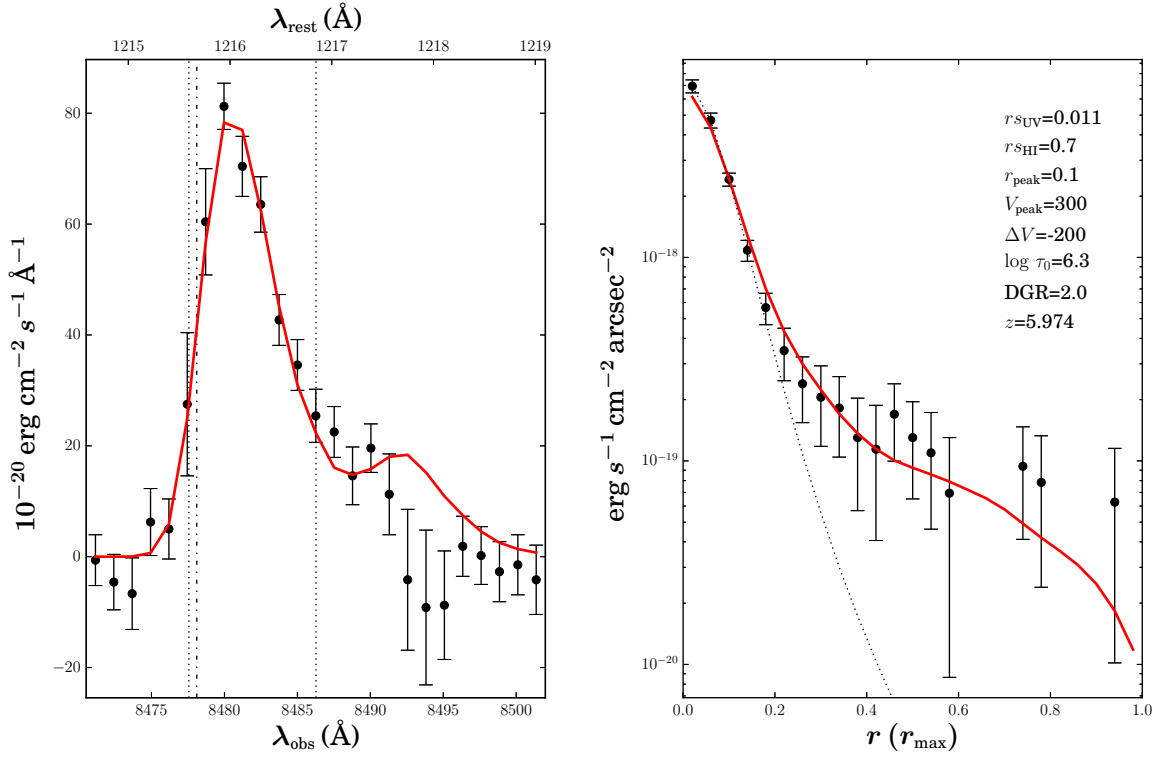


Figure B28:. Similar to Figure 6, but for MUSE #547.

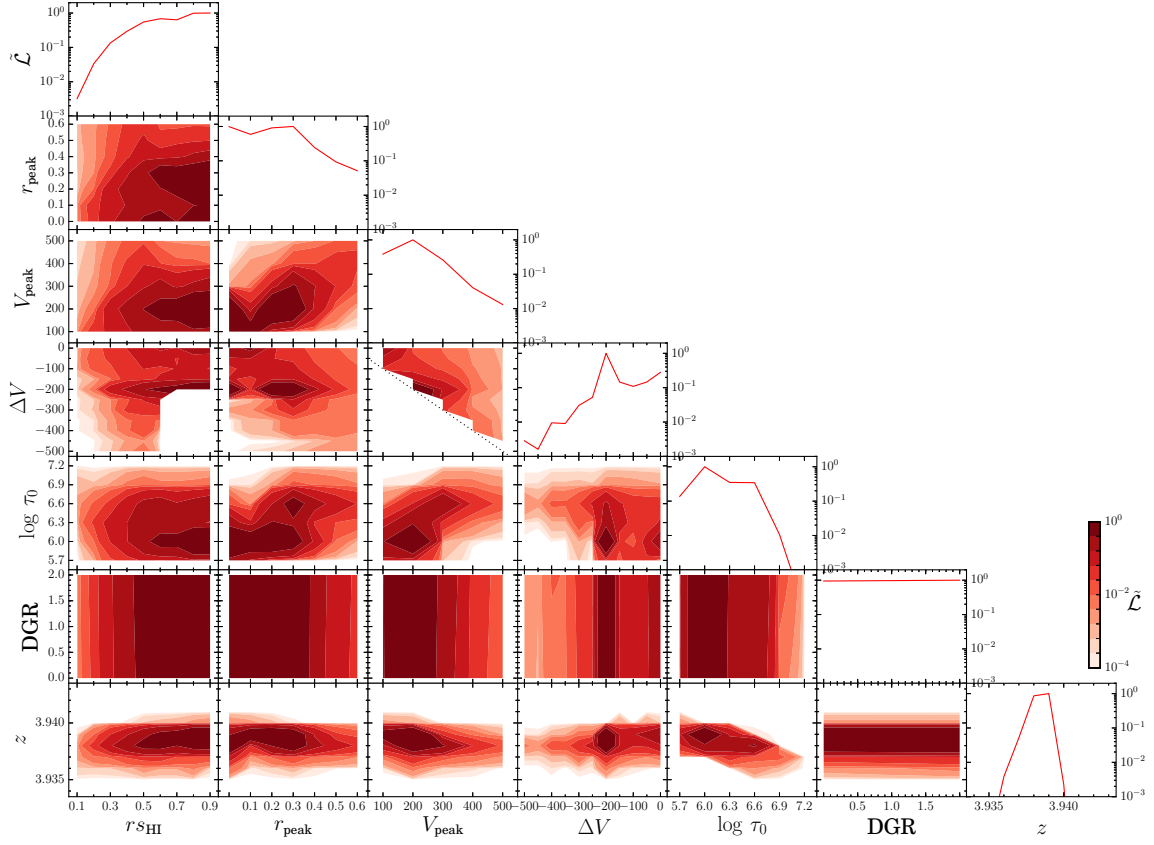


Figure B29:. Similar to Figure 5, but for MUSE #364.

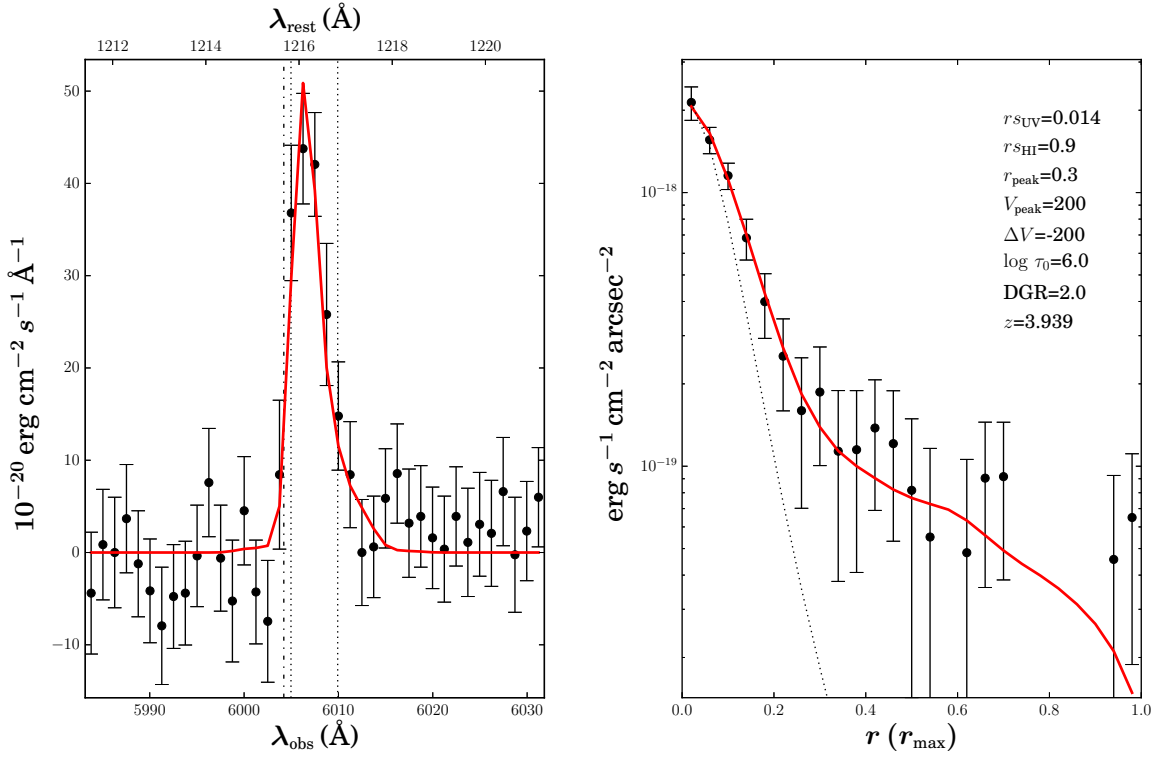
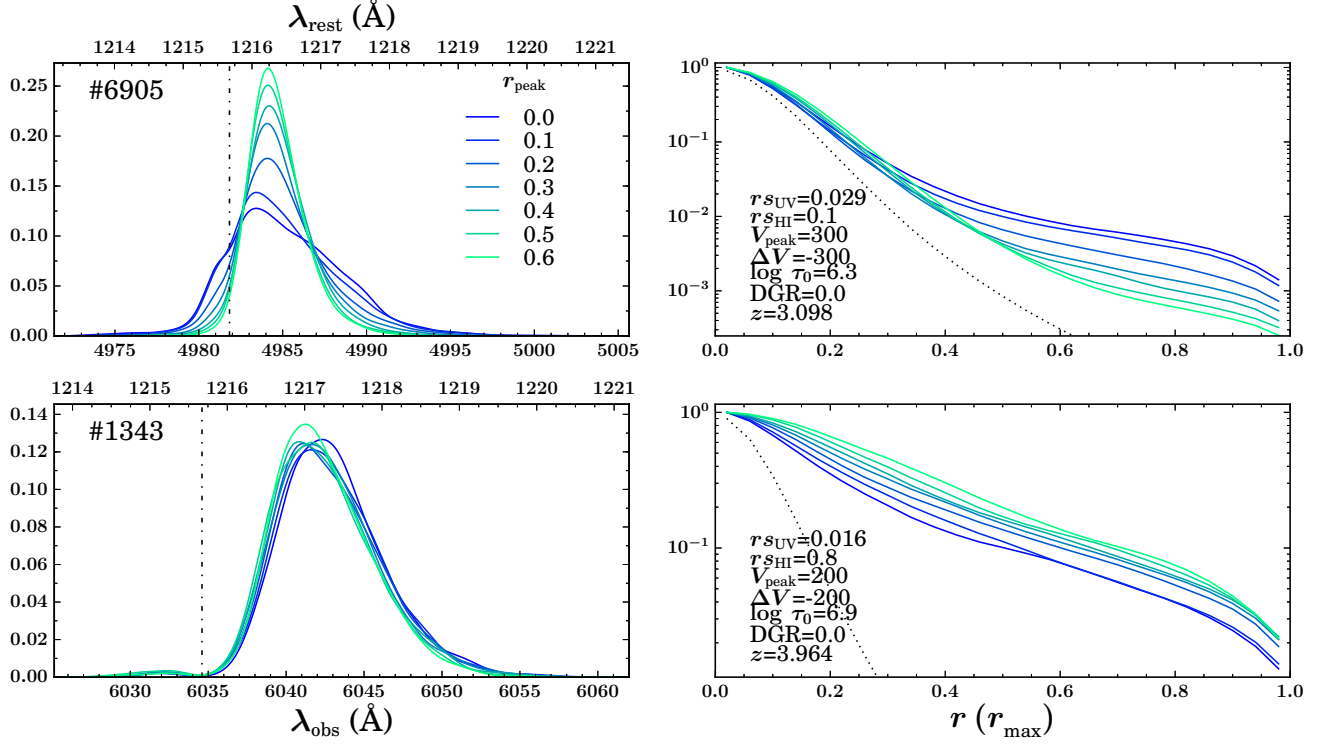
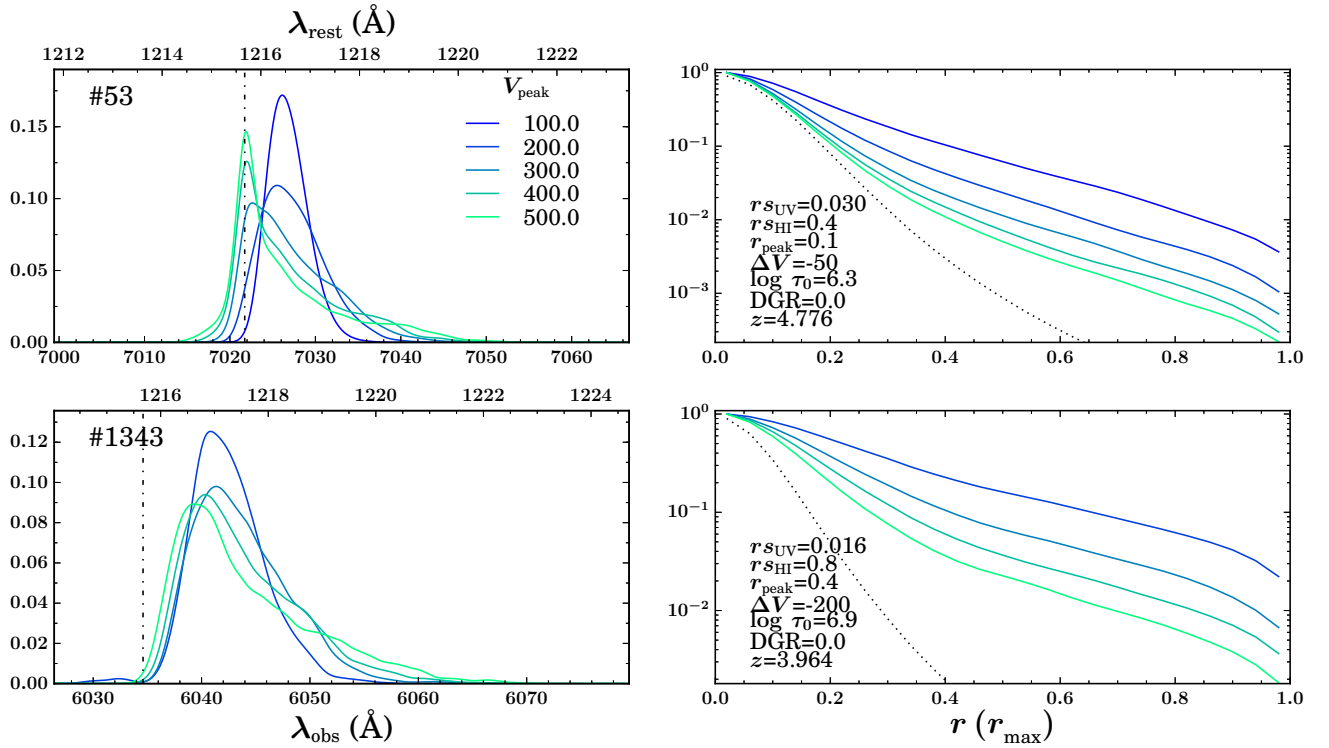


Figure B30:. Similar to Figure 6, but for MUSE #364.

Figure C31:. Similar to Figure 8, but with varying r_{peak} .Figure C32:. Similar to Figure 8, but with varying V_{peak} .

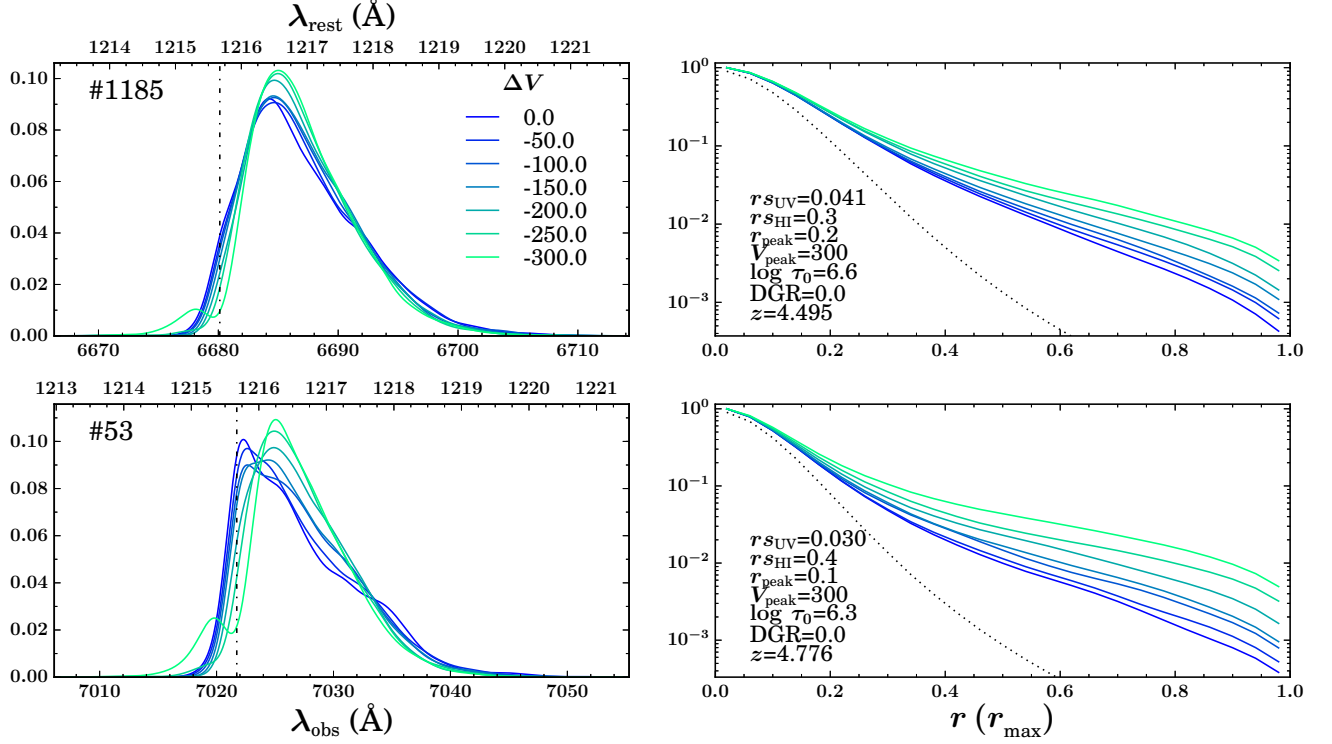


Figure C33.: Similar to Figure 8, but with varying ΔV .

surface brightness profile becomes flatter. This is because photons that were lucky enough not to experience many scatterings in the inner region are more likely to be scattered in the outer region as the medium there becomes more static (i.e., less transparent) with decreasing ΔV . The change of spectrum with ΔV appears less obvious, which can depend on other parameters. Yet, the spectrum tends to have a higher intensity at the central wavelength when ΔV is larger (i.e., larger velocity at the edge). One interesting feature in the spectrum is a small blue bump that appears when the velocity at the edge is zero. This blue bump may consist of lucky photons that have experienced almost no scattering until they reach the edge. However, these photons are scattered by static medium at the edge to either redder or bluer wavelengths than the central wavelength, forming a (symmetric) double-peak spectrum. Because there are not many such lucky photons, such a double-peak feature is subdominant; the red peak of the double-peak spectrum is hidden in the dominant main body and the blue peak appears as a small bump.

Because dust absorbs Ly α photons and re-emits photons at longer wavelengths (i.e., at mid- or far-infrared wavelengths), the main effect of dust is the reduction in the amount of Ly α photons. Meanwhile, the chance of a photon being destructed by dust is proportional to the number of scatterings that the photon has experienced until its escape. Photons at wavelengths far away from the central wavelength are those that have been scattered a lot, and thus they are more likely to interact with dust. Therefore, the intensity at a longer wavelength (in the redder side than the Ly α central wavelength) might be reduced more than that at a shorter wavelength compared to the case without dust, implying that dust could have an impact on the shape of spectrum as well as the absolute intensity level. However, the spectra and surface brightness profiles with different DGRs show not much differences as seen in the panels of upper two rows of Figure 34. It could be because the best-fit parameter set of each target galaxy is not optimal to see the effect of dust on the shapes of spectrum and surface brightness profile. To maximize the dust effect, we use a parameter set that is thought to maximize the number of scatterings (e.g., large τ_0 , large r_{peak} , small V_{peak} , and small ΔV). Now we can see some changes in the spectral shape with DGR in the bottom left panel of Figure 34; larger intensity reduction at long wavelengths when DGR is larger, resulting in a sharper spectrum with its peak closer to the central wavelength. It should be noted that each spectrum is normalized by the amount of escaping photons to compare the spectral shape not the intensity. The overall intensity decreases with DGR, which will be discussed in the following section. The effect of dust on the shape of surface brightness profile appears less significant.

There is one parameter that we have not varied but may have a strong impact on Ly α transfer process, which is

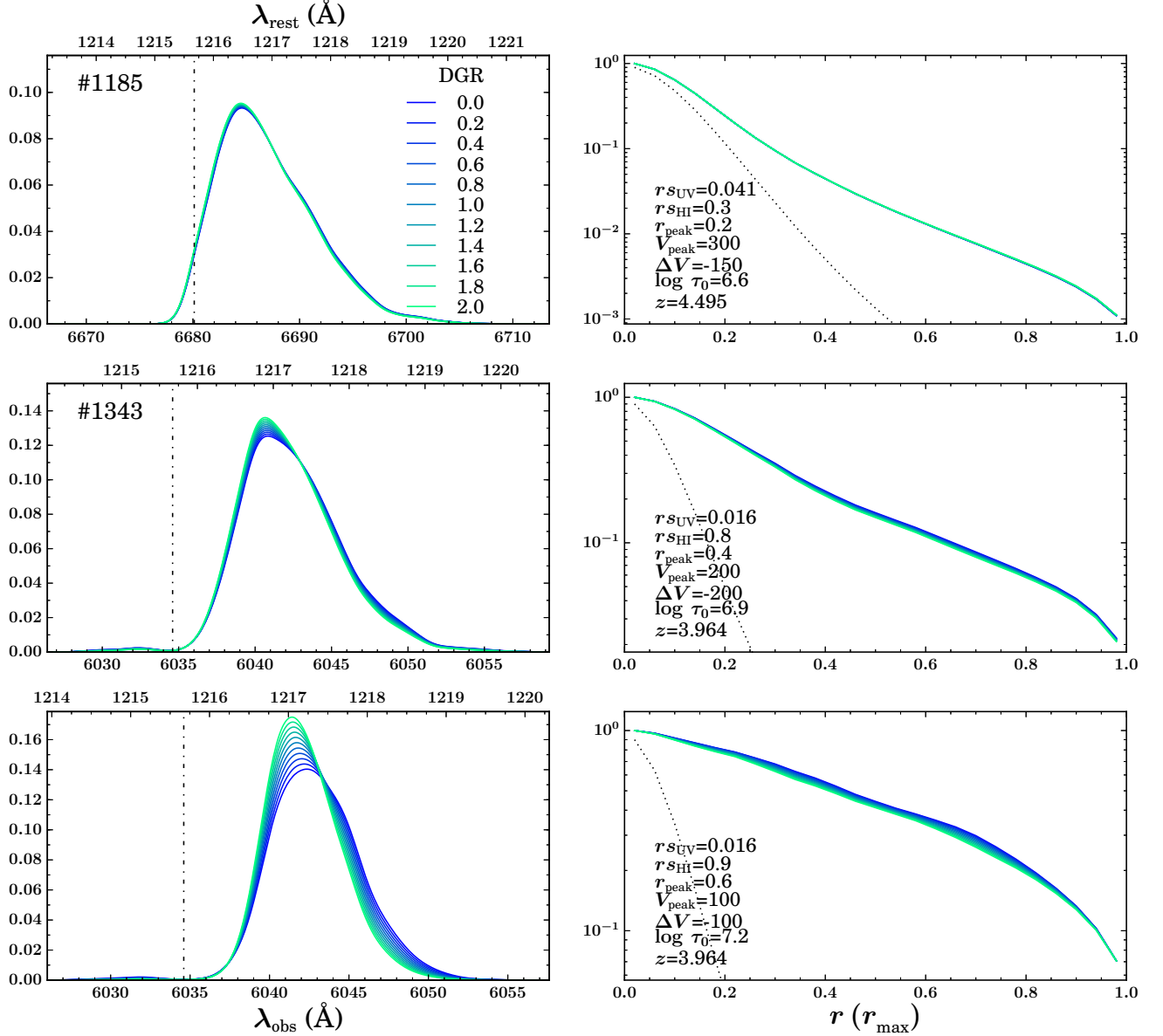


Figure C34.: Panels in the upper two rows are similar to those in Figure 8, but with varying DGR. Panels in the bottom row are with a parameter set that could maximize the number of scatterings (large τ_0 , large r_{peak} , small V_{peak} , and small ΔV), which is adopted to see the impact of dust more clearly.

medium temperature. We fix medium temperature at 10^4K in order to focus on the impact of other parameters such as the scale radius of medium density and parameters for medium velocity profile that have not been studied much so far. However, it is worth checking how medium temperature affects the shapes of emerging Ly α spectrum and surface brightness profile briefly. We perform four additional runs for medium temperature of 10^1 , 10^2 , 10^3 , and 10^5K , fixing other parameters at their best-fit values to MUSE #1185. We note that hydrogen atoms are almost fully ionized at a temperature as high as 10^5K . In our simulation, the medium temperature of 10^5K should be regarded as an effective temperature that includes the effect of turbulent motion. Figure 35 shows that spectrum becomes broader with a larger peak shift and surface brightness profile becomes shallower as medium temperature increases. This is because hydrogen atoms have a broader velocity distribution when medium temperature is higher, and they scatter Ly α photons of a broader frequency range. In the result, high medium temperature leads to more scatterings (under the assumption that the ionization state of hydrogen atoms does not change with temperature). Similar to the case

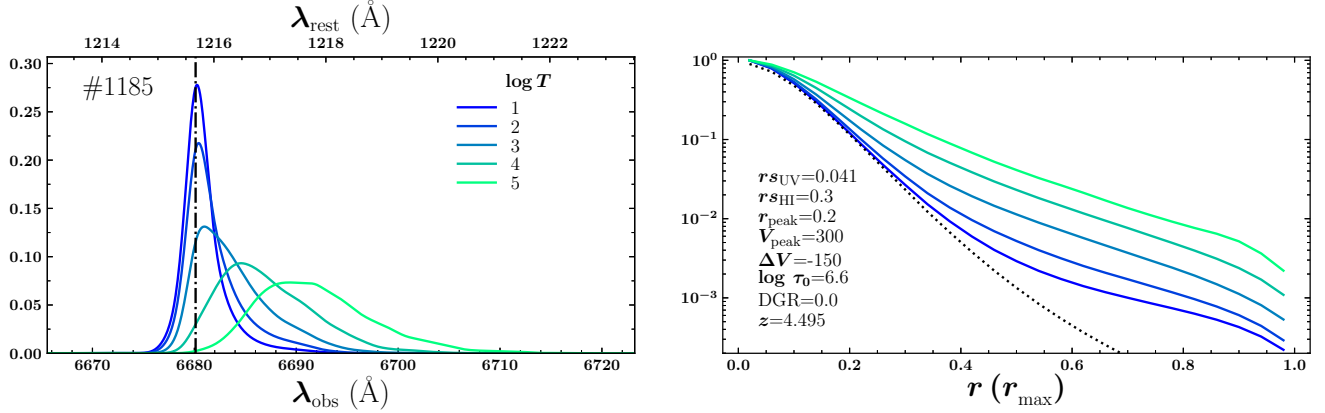


Figure C35:. Similar to Figure 8, but with varying medium temperature.

that we change the input spectrum shown in Section 4.7, the best-fit parameter set for a galaxy will differ if we change medium temperature. Nevertheless, our approach of fixing medium temperature is useful for exploring the impact of other parameters more efficiently because we can reduce the dimension of the parameter space we are exploring and the resulting computation time. It will be our future work to consider medium temperature together with all relevant quantities that include density, pressure, and ionization state to be self consistent.

D. PEAK SHIFT OF LY α SPECTRUM AND PEAK VELOCITY OF MEDIUM

In this section, we examine the impact of the velocity of expanding medium on the emerging spectrum in more detail, assuming an expanding velocity ranging from several tens to several hundreds km s⁻¹. To focus on the impact of medium velocity only, we simplify the models by considering a central, monochromatic source in an expanding H I halo of uniform density (optical depth of 10⁶) and uniform temperature (10⁴K). We adopt three different types of velocity profile: (a) constant expansion, (b) Hubble-like expansion, and (c) accelerated and then decelerated expansion (as in this paper).

Figure 36 shows (left) emerging spectra and (right) the distributions of numbers of scatterings (N_{scatt}) for nine peak expanding velocities (denoted by different colors) for each velocity type (each row). From $V_{\text{peak}} = 0$ to ~ 50 km s⁻¹ the red peak of emerging spectrum appears to be progressively displaced redwards. When $V_{\text{peak}} \gtrsim 50$ km s⁻¹, however, the peak appears closer to the central wavelength (i.e., $x = 0$) as the velocity increases. This trend is consistent with the result shown in Figure 7 of Verhamme et al. (2006). The number of scatterings, on the other hand, consistently decreases as velocity increases, which is attributed to decreased effective optical-depth. Therefore, as the medium velocity is too high, photons will escape without having chances to undergo a large number of scatterings; as a consequence, no significant frequency change is found in the emergent spectrum.

The behavior of spectral peak when $V_{\text{peak}} \lesssim 50$ km s⁻¹ can be understood with the help of the redistribution function, $\mathcal{R}(x_{\text{out}}|x_{\text{in}})$, that describes the probability of the “out” frequency (x_{out}) after a single scattering for a given “in” frequency (x_{in} , the frequency before scattering)⁸. Figure 21 of Dijkstra (2017) shows that when the input frequency is farther away from the central frequency, so is the output frequency. As the velocity of the medium is larger, the input frequency is shifted farther away from the central frequency in the medium frame, which will end up with larger frequency change after a number of scatterings, despite decreased effective optical-depth. It should be noted, however, that such an effect can happen for low medium velocities where enough number of scatterings can still occur; i.e., $V_{\text{peak}} \lesssim 50$ km s⁻¹ in our particular example. This critical expanding-velocity will depend on the optical depth, temperature of medium, and the input spectrum.

E. CORRELATION BETWEEN EXTENT OF LY α SOURCE AND LY α HALO

Figure 37 shows a correlation between $r_{s_{\text{halo}}}/r_{s_{\text{cont}}}$ and $r_{s_{\text{cont}}}$ for eight target galaxies of this study (filled black circles) and for the full sample of L17 (filled black circles and open gray circles altogether). $r_{s_{\text{halo}}}/r_{s_{\text{cont}}}$ is strongly anticorrelated with $r_{s_{\text{cont}}}$ (refer to the Spearman rank-order correlation coefficients and p -values given in the figure). It should be noted that this anticorrelation between $r_{s_{\text{halo}}}/r_{s_{\text{cont}}}$ and $r_{s_{\text{cont}}}$ is not derived from the simulation results,

⁸ Refer to Section 7.3 of Dijkstra (2017) for more details.

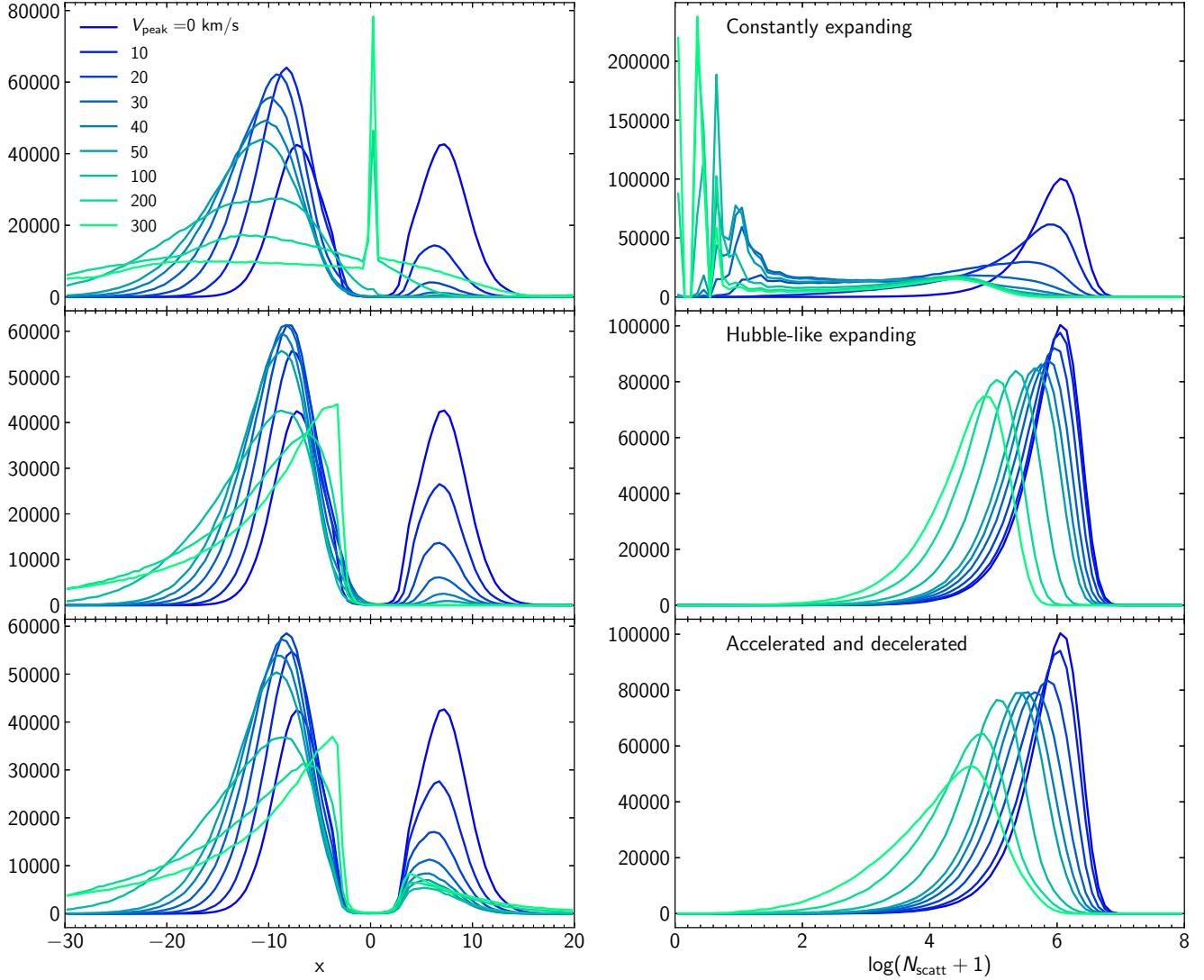


Figure D36.: Spectra (left panels) and numbers of scatterings (right panels) of photons that emerge from a central monochromatic source in an expanding H I halo of uniform density (optical depth of 10^6) and uniform temperature ($10^4 K$), for nine peak expanding velocities (denoted by different colors) for three different velocity types: constantly expanding (top), Hubble-like expanding (middle), and accelerated and then decelerated expanding (bottom, $r_{\text{peak}} = 0.5$ and $\Delta V = -V_{\text{peak}}$).

but from the observational results. This anticorrelation is interesting because $r_{s_{\text{halo}}}$ itself is positively correlated with $r_{s_{\text{cont}}}$ (see Figure 13 in L17). The positive correlation between $r_{s_{\text{halo}}}$ and $r_{s_{\text{cont}}}$ simply indicates that Ly α photons are generated where UV photons are (i.e., H II regions) through photoionization followed by recombination. However, the anticorrelation between $r_{s_{\text{halo}}}/r_{s_{\text{cont}}}$ and $r_{s_{\text{cont}}}$ implies that the $r_{s_{\text{halo}}}-r_{s_{\text{cont}}}$ correlation is not that strong but rather relatively weak. This weakness in the $r_{s_{\text{halo}}}-r_{s_{\text{cont}}}$ relationship suggests that other factors than $r_{s_{\text{cont}}}$ will be more critical in determining $r_{s_{\text{halo}}}$; the factor that mostly matters the size of Ly α halo would be how significantly the Ly α photons diffuse out in space by resonance scattering, rather than the spatial size of Ly α source.

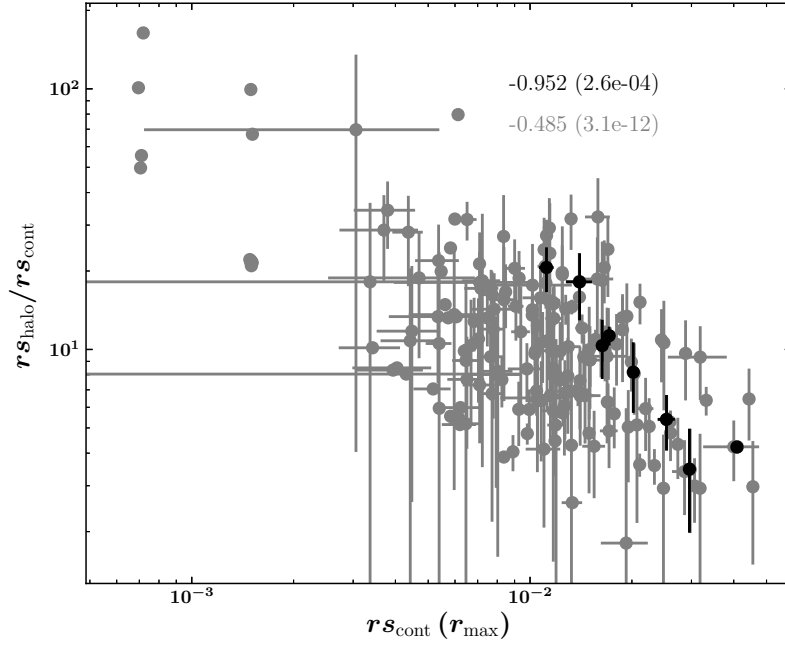


Figure E37:. Anticorrelation between $rs_{\text{halo}}/rs_{\text{cont}}$ and rs_{cont} of eight target galaxies (filled black circles) and of the full sample of L17 (filled black circles and open gray circles). The Spearman rank-order correlation coefficients and p-values (in the parenthesis) for these two samples are given in the top right panel.